



AFRL-RQ-WP-TR-2016-0130

ELECTRON ENERGY DISTRIBUTION AND TRANSFER PHENOMENA IN NON-EQUILIBRIUM GASES

Steven F. Adams and Bradley S. Sommers

**Electrical Systems Branch
Power and Control Division**

Charles Q. Jiao

UES, Inc.

SEPTEMBER 2016

Final Report

**DISTRIBUTION STATEMENT A: Approved for public release.
Distribution is unlimited.**

See additional restrictions described on inside pages

**AIR FORCE RESEARCH LABORATORY
AEROSPACE SYSTEMS DIRECTORATE
WRIGHT-PATTERSON AIR FORCE BASE, OH 45433-7541
AIR FORCE MATERIEL COMMAND
UNITED STATES AIR FORCE**

NOTICE AND SIGNATURE PAGE

Using Government drawings, specifications, or other data included in this document for any purpose other than Government procurement does not in any way obligate the U.S. Government. The fact that the Government formulated or supplied the drawings, specifications, or other data does not license the holder or any other person or corporation; or convey any rights or permission to manufacture, use, or sell any patented invention that may relate to them.

This report was cleared for public release by the USAF 88th Air Base Wing (88 ABW) Public Affairs Office (PAO) and is available to the general public, including foreign nationals.

Copies may be obtained from the Defense Technical Information Center (DTIC)
(<http://www.dtic.mil>).

AFRL-RQ-WP-TR-2016-0130 HAS BEEN REVIEWED AND IS APPROVED FOR
PUBLICATION IN ACCORDANCE WITH ASSIGNED DISTRIBUTION STATEMENT.

*//Signature//

STEVEN F. ADAMS
Program Manager
Electrical Systems Branch
Power and Control Division

//Signature//

GREGORY L. FRONISTA
Branch Chief
Electrical Systems Branch
Power and Control Division

//Signature//

BRYAN J. CANNON
Principal Scientist
Power and Control Division
Aerospace Systems Directorate

This report is published in the interest of scientific and technical information exchange and its publication does not constitute the Government's approval or disapproval of its ideas or findings.

*Disseminated copies will show “//Signature//” stamped or typed above the signature blocks.

REPORT DOCUMENTATION PAGE				Form Approved OMB No. 0704-0188	
<p>The public reporting burden for this collection of information is estimated to average 1 hour per response, including the time for reviewing instructions, searching existing data sources, gathering and maintaining the data needed, and completing and reviewing the collection of information. Send comments regarding this burden estimate or any other aspect of this collection of information, including suggestions for reducing this burden, to Department of Defense, Washington Headquarters Services, Directorate for Information Operations and Reports (0704-0188), 1215 Jefferson Davis Highway, Suite 1204, Arlington, VA 22202-4302. Respondents should be aware that notwithstanding any other provision of law, no person shall be subject to any penalty for failing to comply with a collection of information if it does not display a currently valid OMB control number. PLEASE DO NOT RETURN YOUR FORM TO THE ABOVE ADDRESS.</p>					
1. REPORT DATE (DD-MM-YY) September 2016		2. REPORT TYPE Final		3. DATES COVERED (From - To) 15 March 2010 – 16 September 2016	
4. TITLE AND SUBTITLE ELECTRON ENERGY DISTRIBUTION AND TRANSFER PHENOMENA IN NON-EQUILIBRIUM GASES				5a. CONTRACT NUMBER In-house	
				5b. GRANT NUMBER	
				5c. PROGRAM ELEMENT NUMBER 61102F	
6. AUTHOR(S) Steven F. Adams and Bradley S. Sommers (AFRL/RQQE) Charles Q. Jiao (UES, Inc.)				5d. PROJECT NUMBER 2301	
				5e. TASK NUMBER	
				5f. WORK UNIT NUMBER Q126	
7. PERFORMING ORGANIZATION NAME(S) AND ADDRESS(ES) Electrical Systems Branch (AFRL/RQQE) Power and Control Division Air Force Research Laboratory, Aerospace Systems Directorate Wright-Patterson Air Force Base, OH 45433-7541 Air Force Materiel Command, United States Air Force				8. PERFORMING ORGANIZATION REPORT NUMBER AFRL-RQ-WP-TR-2016-0130	
9. SPONSORING/MONITORING AGENCY NAME(S) AND ADDRESS(ES) Air Force Research Laboratory Aerospace Systems Directorate Wright-Patterson Air Force Base, OH 45433-7541 Air Force Materiel Command United States Air Force				10. SPONSORING/MONITORING AGENCY ACRONYM(S) AFRL/RQQE	
				11. SPONSORING/MONITORING AGENCY REPORT NUMBER(S) AFRL-RQ-WP-TR-2016-0130	
12. DISTRIBUTION/AVAILABILITY STATEMENT DISTRIBUTION STATEMENT A: Approved for public release. Distribution is unlimited.					
13. SUPPLEMENTARY NOTES PA Case Number: 88ABW-2016-3960; Clearance Date: 10 Aug 2016. The U.S. Government is joint author of this work and has the right to use, modify, reproduce, release, perform, display, or disclose the work.					
14. ABSTRACT During this 3-year in-house experimental research task, researchers in the Electrical Systems Branch of the Air Force Research Laboratory (AFRL/RQQE) applied advanced spectroscopic and laser techniques to measure, monitor and ultimately control the distribution of electronic and kinetic energies within low temperature plasmas and enhance the understanding of phenomena associated with non-equilibrium energy distributions. The experimental results from this task provided insight into the potential for further technological advancements, including plasma switching, ignition enhancement, laser medium excitation, and plasma surface treatments. Advances in kinetic modeling have also generated accurate computations that represent the energy-dependent behavior of charged species in the non-equilibrium environment and have allowed the simulation of breakdown phenomena in potential Air Force applications. Specifically, measurement techniques of temperatures and energy distributions within micro-discharges were developed and optimized, advanced multi-photon absorption and ionization techniques for both diagnostics and pre-ionization seeding for gas breakdown were analyzed, and ion chemistry leading to ignition of advanced fuel molecules was investigated. The experimental approaches applied include advanced ultraviolet spectroscopic techniques with methods in subtractive triple-grating spectroscopy, laser scattering techniques, optical emission spectroscopy, multi-photon laser techniques to both detect and stimulate laboratory gas systems, and finally Fourier transform mass spectroscopy for ion analysis. The experimental results focus on laser scatter diagnostics of air microdischarge kinetics, resonant laser induced breakdown of air for fuel-air ignition, and ion chemistry analysis of fuel molecules.					
15. SUBJECT TERMS laser scatter, microplasma, laser ignition, fuel ionization, electron-ion impact					
16. SECURITY CLASSIFICATION OF:			17. LIMITATION OF ABSTRACT: SAR	18. NUMBER OF PAGES 47	19a. NAME OF RESPONSIBLE PERSON (Monitor) Steven F. Adams
a. REPORT Unclassified	b. ABSTRACT Unclassified	c. THIS PAGE Unclassified			19b. TELEPHONE NUMBER (Include Area Code) N/A

TABLE OF CONTENTS

Section	Page
LIST OF FIGURES	ii
LIST OF TABLES	ii
ACKNOWLEDGMENTS	iii
1 SUMMARY	1
1.1 Laser Scatter in Microplasma Summary	1
1.2 Laser Ignition Summary	1
1.3 Ion Chemistry of Fuels Summary	2
2 INTRODUCTION.....	3
2.1 Laser Scatter in Microplasma.....	3
2.2 Laser Ignition	4
2.3 Ion Chemistry of Fuels	5
3 EXPERIMENTAL	6
3.1 Laser Scatter in Microplasma Experiment	6
3.1.1 Direct Current Plasma Jet	6
3.1.2 Glow Discharge Setup	8
3.1.3 Laser Scatter Techniques	9
3.1.4 Triple Grating Spectrometer	9
3.1.5 Optical Setup.....	10
3.2 Laser Ignition Experiment	11
3.3 Ion Chemistry of Fuels Experiment	12
4 RESULTS	18
4.1 Laser Scatter in Microplasma Results.....	18
4.1.1 Rayleigh Scattering.....	18
4.1.2 Rotational Raman Scattering	19
4.1.3 Temperature Measurements in the Plasma Jet.....	21
4.1.4 Temperature Measurements in the Glow Discharge.....	22
4.2 Laser Ignition Results	24
4.3 Ion Chemistry of Fuels Results	27
4.3.1 Electron Ionization.....	27
4.3.2 Ion-molecule Reactions	31
5 CONCLUSIONS	36
5.1 Laser Scatter in Microplasma Conclusions	36
5.2 Laser Ignition Conclusions	36
5.3 Ion Chemistry of Fuels Conclusions	37
6 REFERENCES.....	38

LIST OF FIGURES

Figure	Page
Figure 1: Plasma Jet Body, Integrated into the Accompanying Electrical Circuit	7
Figure 2: Diagram and Image of the Plasma Jet	8
Figure 3: Diagram of the D.C. Glow Discharge Setup	9
Figure 4: Light Incident on the TGS Entrance.....	10
Figure 5: Laser Beam (along y) Imaged at 90° onto the TGS Entrance Slit (along x).....	11
Figure 6: Diagram of Experimental Setup of Laser-induced Ignition Gap	12
Figure 7: Photograph of FTMS System (left) and Cutaway Showing the Internal Electron Gun and Trapping Cube (right).....	13
Figure 8: Schematic of FTMS Apparatus for Electron Impact Ionization Studies	13
Figure 9: Functional Diagram of Ion Excitation and Detection with Example Ion Signals	14
Figure 10: Diagram of Modified Ion Trapping Cell with Screen Electrodes that Trap Ions.....	14
Figure 11: Temporal Sequence of the Ionization and Detection within the FTMS.....	15
Figure 12: Diagram of Sequence for the Ion Plus Parent Molecule Reaction Analysis	16
Figure 13: Obtained Gas Temperature T_g	18
Figure 14: Example 1D T_g Profile	19
Figure 15: Typical Raman Spectra Taken at a Slit Width of 150 μm	20
Figure 16: Gas Temperature within the Plasma Jet	21
Figure 17: Axial and Radial Temperature Profiles in the Plasma Jet.....	22
Figure 18: Radial Temperature Profiles Taken in the Pin-pin D.C. Glow Discharge at Two Separate Operating Conditions (left) 4.0 mA and (right) 8.0 mA	23
Figure 19: Digital Camera Image of Laser-induced Ignition.....	25
Figure 20: High-speed Images of Laser-induced Arc in Air and Air-propane	25
Figure 21: Plot of Breakdown Voltage Threshold.....	26
Figure 22: Gated Images and Spectra with 10 ns Resolution	27
Figure 23: A High-resolution Mass Spectrum at m/z 26 Showing Multiple Isobaric Ions	28
Figure 24: Total Electron Ionization Cross Section of TEB.....	29
Figure 25: Log plots of Partial Cross Sections for Major Product Ions from Electron Ionization of TEB	30

LIST OF TABLES

Table	Page
Table 1: Gas-phase Ion-molecule Reactions of TEB with Selected Ions from Electron Ionization of TEB	32

ACKNOWLEDGMENTS

The authors received incredible support from many individuals within the Electrical Systems Branch including B. Allen Tolson for his technical expertise and guidance, Amber Hensley for her scientific and administrative support, and Vladimir Demidov for scientific and technical guidance. This work was funded by the Air Force Office of Scientific Research under the Laboratory Research Initiation Request (LRIR) task 13RQ13COR managed by John Luginsland and Jason Marshall.

1 SUMMARY

During this three year in-house experimental research task, researchers in the Electrical Systems Branch of the Air Force Research Laboratory (AFRL/RQQE) have applied advanced spectroscopic and laser techniques to measure, monitor and ultimately control the distribution of electronic and kinetic energies within low temperature plasmas and enhance the understanding of phenomena associated with non-equilibrium energy distributions. The experimental results from this task have helped examined the potential for further technological advancements, including areas of interest to the Air Force such as plasma switching, ignition enhancement, laser medium excitation and plasma surface treatments. Advances in kinetic modeling have also generated accurate computations that represent the energy dependent behavior of charged species in the non-equilibrium environment and have allowed the simulation of breakdown phenomena in potential Air Force applications. Specifically, measurement techniques of temperatures and energy distributions within micro-discharges were developed and optimized, advanced multi-photon absorption and ionization techniques for both diagnostics and pre-ionization seeding for gas breakdown were analyzed, and ion chemistry leading to ignition of advanced fuel molecules was investigated. The experimental approaches applied include advanced ultraviolet spectroscopic techniques with methods in subtractive triple-grating spectroscopy, laser scattering techniques, optical emission spectroscopy, multi-photon laser techniques to both detect and stimulate laboratory gas systems, and finally Fourier transform mass spectroscopy for ion analysis. The analyses of these data have been directed toward Air Force technology development including plasma switches, plasma interactions with materials, novel applications of atmospheric micro-discharges, plasma assisted combustion, and fuel development with enhanced ion chemistry. The experimental results highlighted in this report focus on the following topics: laser scatter diagnostics of air microdischarge kinetics, resonant laser induced breakdown of air for fuel-air ignition, and ion chemistry analysis of fuel molecules.

1.1 Laser Scatter in Microplasma Summary

A laser scattering system utilizing an ultraviolet laser with a triple grating spectrometer was assembled in order to measure gas temperature in atmospheric plasma sources. Such laser scattering interactions offer a non-invasive technique for investigating atmospheric microplasma sources, which have potential applications in remote optical sensing, materials processing, and environmental decontamination. This particular system was unique in that it utilizes an ultraviolet laser line (266 nm), which increased the cross section for Rayleigh and Raman scattering by a factor of 16 in comparison to the more common 532 nm laser operating in the visible range. In this work, the laser scattering system was used to directly compare the rotational gas temperature (T_r) and gas kinetic temperature (T_g) in two different atmospheric plasma sources: (1) a direct current plasma jet operating on nitrogen and (2) a conventional pin-pin glow microdischarge in air. Results showed agreement between T_r and T_g both in the low temperature afterglow of the plasma jet (300-700 K) and the hot center of the atmospheric glow (1500-2000 K). These observations lent credence to the common assumption of rotational relaxation in atmospheric plasmas and validated the ultraviolet laser diagnostic for future application in atmospheric microplasma sources.

1.2 Laser Ignition Summary

A resonant multi-photon scheme was investigated that could provide laser-induced ignition within a high-voltage gap across an aircraft combustion chamber. The resonant technique could

potentially be applied as a laser trigger from a compact low power laser source leading to breakdown and ignition of an aircraft air-fuel flow. Experiments with resonant laser-induced ignition of a moderate-speed flow of an air-propane mixture were conducted by applying a high voltage across the flow chamber that was significantly less than normal self-breakdown. The resulting spark followed the laser pre-ionized path across the chamber within a few microseconds of the laser pulse which led to ignition and combustion on the time scale of milliseconds. This laser scheme involves resonant enhanced multi-photon ionization (REMPI) and subsequent laser field-enhanced electron avalanche to generate a pre-ionized micro-plasma path between flow chamber walls and thus guide the ignition spark through fuel-rich areas of the air-fuel flow. It was determined that a specific resonant ultraviolet wavelength, 287.5 nm, was optimal at relatively low laser pulse energy to photo-ionize oxygen molecules in a fuel-air flow to reliably initiate ignition. This laser wavelength coincides with a 2+1 REMPI transition in molecular oxygen. With this resonant method, sufficient photo-ionization and laser field-enhanced electron avalanche ionization have been generated for inducing air breakdown at a relatively low laser power compared to most laser breakdown concepts. This low power requirement may allow for a laser source to be transmitted to an ignition chamber via fiber optic coupling. Results of this study include detailed spectroscopy of the evolution of the optical emission from laser pre-ionization, spark, and eventual ignition. Spectroscopic results were compared to breakdown in pure air to determine the role of the 2+1 REMPI transition in molecular oxygen compared to hydrocarbon dissociation and ionization processes that may aid ignition. In addition, high speed photography of flame ignition in an air-propane flow was conducted, showing the spatial and temporal evolution of the laser-induced spark and flame kernel leading to combustion.

1.3 Ion Chemistry of Fuels Summary

The absolute total and partial cross sections of electron ionization on triethylborane (TEB) were measured in an electron energy range of 6.6-200 eV. The total cross section reached a maximum of $2.2 \times 10^{-15} \text{ cm}^2$ in 65-85 eV energy region. Product ions from the electron ionization included $\text{C}_2\text{H}_{2.5}^+$, BCH_4^+ , $\text{BC}_2\text{H}_{2,4,6}^+$, $\text{BC}_3\text{H}_{4,6}^+$, $\text{BC}_4\text{H}_{8,10}^+$ and $\text{BC}_6\text{H}_{15}^+$, among which $\text{BC}_6\text{H}_{15}^+$, $\text{BC}_4\text{H}_{10}^+$ and BC_2H_6^+ were the most abundant ions. Gas-phase reactions between TEB and certain major ions from the electron ionization of TEB were studied. Common products from the ion-molecule reactions were $\text{BC}_4\text{H}_{10}^+$ and BC_2H_6^+ , as well as association products for certain heavy-ion reactions. The mechanisms of forming $\text{BC}_4\text{H}_{10}^+$ and BC_2H_6^+ in ion-molecule reactions are believed to be simple ethide transfer and ethide transfer followed by dissociation (loss of C_2H_4), respectively.

2 INTRODUCTION

2.1 Laser Scatter in Microplasma

Atmospheric microplasma sources have been investigated for a variety of applications, including plasma aided combustion, fuel reforming, and environmental decontamination [1]. The development of non-invasive diagnostic techniques capable of measuring plasma component properties, such density and temperature remains essential to the development of practical devices [2]. Component temperatures in atmospheric plasmas can be measured using direct laser scattering techniques utilizing Rayleigh, Raman, and Thomson scattering interactions with spatial resolution below 100 μm [3]. This makes scattering an ideal diagnostic for the typical micro plasma source geometry. Experiments utilizing laser scattering have recently been applied to atmospheric plasma devices ranging from microwave plasma jets [4] to high pressure dc glow microdischarges [5]. In all of these cases, the laser wavelength is chosen in the visible range (typically 532 nm). This is largely due to the ease of integration with conventional optical components and imaging equipment. It is also beneficial for distinguishing the low intensity Thomson signal from the much stronger Rayleigh signal.

In this report, we utilize an ultraviolet laser scattering system operating at 266 nm. The UV line was chosen to maximize the cross section for Rayleigh and Raman scattering, which scales as $1/\lambda^4$ [6]. This provides a factor of 16 increase in signal strength over a similar system operating at 532 nm. This system is used to develop two diagnostics: (1) direct measurement of gas temperature (T_g) by Rayleigh scattering and (2) direct measurement of rotational temperature (T_r) by Raman scattering. These measurements are performed in two separate atmospheric plasma sources: (1) a direct current plasma jet composed of chemically reactive species with temperatures in the range 300-700 K and (2) a conventional direct current microscale glow discharge, with temperatures in the range 1500-2000 K. Both sources were developed at the Air Force Research laboratory at Wright Patterson AFB.

In these plasma sources it is commonly assumed that the rotational temperature and gas kinetic temperature are equal. This is due to the high neutral collision frequency at atmospheric pressure, which leads to the rapid exchange between the kinetic energy (20-100 meV) and rotational levels (~ 1 meV) of the molecules. Temperature measurements obtained in each source will be used to test the assumption of equilibrium in these devices, as well as validate both diagnostics as a measurement of gas temperature. Direct current atmospheric plasma jets have garnered interest for their ability to produce chemically reactive species for applications in processing and etching, particularly as an alternative to pulsed jet systems, which require expensive feed gas and complex electrical components [7]. Along with a plasma jet, a more conventional atmospheric D.C. discharge was also developed in this work for comparison, which consisted of a glow discharge with pin-pin electrodes.

2.2 Laser Ignition

A variety of methods can be used to initiate breakdown in air, leading to various controlled spark applications such as high current spark-gap switching or the ignition of an air-fuel mixture within a combustion system. The most common mechanisms to induce breakdown in air is the production of high-tension sparks by conventional induction coils or production of high-energy and very high temperature sparks produced by a condenser discharge. There has been some research and development of laser triggered breakdown technology intended for the eventual replacement of spark-plug igniters with laser ignition systems in combustion chambers [8]. Most of this previous work has involved very high power pulsed lasers that cause high-field breakdown of air and photoelectron effects at an electrode surface. For combustion ignition, the practical issues of gaining optical access to the ignition volume and integrating a high power pulsed laser near a combustion engine has been a concern [9]. An attractive concept is the guidance of a lower power laser pulse via fiber-optic cable into the ignition region that still reliably induces breakdown of the air-fuel mixture. Ignition induced by a fiber coupled laser could possibly be realized by keeping the required laser power low through efficient volume ionization with the laser tuned to the proper wavelength to achieve resonant-enhanced multiphoton ionization (REMPI) [10, 11].

In previous experiments, the induced breakdown of an air gap with an applied high voltage has been investigated with a novel ultraviolet laser triggering scheme which has been demonstrated to provide both spatial and temporal precision to the resulting arc [10]. The flowing air gap, in its initial off-state, consisted of two electrodes, separated by a variable spaced ignition gap ($d = 1$ cm to 5 cm) which was set to a sufficient distance that it did not spontaneously break down under the applied voltage. It is well known that self-breakdown in dry atmospheric air will occur at an electric field threshold of about $E_b = 30$ kV/cm with a gap on the order of $d \sim 1$ cm, with this threshold slowly decreasing with increasing gap distances [12]. It is also known that the creation of a localized increase in the electric field, or field distortion, within the gap can trigger breakdown even with an applied voltage less than the self-breakdown threshold. Introducing such an electric field distortion within the gap at a specific time and specific location could provide precise guidance of when and where the ignition spark will occur. These previous experiments demonstrated that electric field distortion could be induced within an ignition gap by the application of focused laser energy which ionized a channel of flowing gas within a gap [10]. In this laser technique, the laser path passed through an aperture in the anode and was directed across the gap to strike the cathode. This allowed a pre-ionized channel to form along the laser path between the electrodes, forming a space charge region and local field distortion. Within this region of high field near the electrode there was a greater rate of direct electron impact ionization. If the resulting field distortion was sufficient to sustain electron avalanche across the entire gap, then breakdown occurred and a high current resulted along the laser path [13]. Additionally, to demonstrate the precision guidance of the laser induced breakdown technique, the laser was propagated across the ignition gap at an angle up to 40° to the electric field lines with the resulting arc followed the laser path and not the applied field lines.

This laser excitation technique involved a focused pulsed laser at a specific ultraviolet wavelength to induce REMPI within an electrode gap. With this resonant method, sufficient photo-ionization was generated for inducing air breakdown at a relatively low laser power compared to most laser breakdown concepts. This low power requirement may allow for a

compact laser ignition source consisting of a solid state laser and fiber optics for convenient optical access to the ignition chamber.

The particular resonant laser transition that allowed induced breakdown in the flowing air gap involved a little studied REMPI transition in molecular oxygen. A two-photon transition initially excites the ground state $O_2(X^3\Sigma)$ molecule to the $O_2(C^3\Pi, v=2)$ excited state, which is found to have a maximum transition strength at a wavelength of 287.5 nm [14]. From the $O_2(C)$ state, a third photon within the same laser pulse readily ionizes the O_2 , creating significant ions and electrons in the laser focus region in dry or humid air at atmospheric pressure [10,11]. This scheme is termed a 2+1 photon REMPI process within molecular oxygen. The $O_2(C^3\Pi, v=2)$ excited state is known to be a relatively short-lived state that nominally pre-dissociates after a few picoseconds. It is possible that in atmospheric air, though, the $O_2(C)$ is transferring its energy via collision to the $N_2(a'^1\Sigma_u, v=1)$ metastable state, which has a coincident term energy. If transfer occurs during the laser pulse then the much longer lived $N_2(a')$ could help sustain the REMPI process through the $O_2(C)$ intermediate state.

In this work, the 2+1 photon REMPI process with a pulsed 287.5 nm laser is applied to a flowing air or air-propane mixture in the open laboratory air through an electrode gap. Laser-induced ignition events are studied for various applied voltages across the gap. Spectroscopic results are compared to breakdown in pure air to determine the role of the 2+1 REMPI transition in molecular oxygen compared to hydrocarbon dissociation and ionization processes that may aid ignition. In addition, high speed photography of flame ignition in an air-propane flow was conducted, showing the spatial and temporal evolution of the laser-induced spark and flame kernel leading to combustion.

2.3 Ion Chemistry of Fuels

Boron-containing compounds are distinctive electron-deficient species and are therefore of great interest in basic research because of their unusual chemistries.[15,16] While the development of boron chemistry is still in its infant stage compared to organic chemistry, it has become an exciting research field in recent decades.[17,18] Boron-containing compounds are also finding an increasing number of applications. Alkylboranes, mainly triethylborane (TEB), have been used as radical initiators in many chemical reactions because of their ability to yield alkyl radicals in the presence of oxygen molecule.[19-23] TEB is an excellent ignition source for liquid fuel ramjet combustor and is used as a hypergolic igniter in air-breathing jet engines and rocket engines.[24-27]

Aimed toward providing more data to understand basic boron chemistry and plasma processes involving TEB; this paper reports our recent study on the electron ionization of TEB and the reactions of the ions from TEB with their parent molecule. Total and partial ionization cross sections and ion-molecule reaction rates are presented, and the reaction mechanisms of forming major product ions are discussed.

3 EXPERIMENTAL

Throughout the three year in-house experimental research task, AFRL/RQQE scientists and engineers conducted research in the Energy Sciences Facility in Building 23, Wright-Patterson AFB, OH, which was completed in 2012 under a 25 million dollar Military Construction Project entitled “Advanced Power and Thermal Research Laboratory”. The project involved the complete interior renovation of Building 23. The historical Building 23, originally constructed in 1934, is located immediately adjacent to the AFRL Power and Control Division’s main campus and has been transformed into a modern laboratory facility designed to encourage innovation and collaboration. The completely redesigned facility includes areas for materials processing, data acquisition, clean rooms, dry room, and fabrication facilities.

The space dedicated to this AFOSR task includes three well equipped laboratory rooms on the third floor of Building 23 with a total area of over 3,000 square feet. Each laboratory room was originally designed and built according to specifications derived from the previous AFOSR task requirements, including extended rooms for laser experiments, chilled water, pump ventilation, shop air, overhead electrical power, fume hoods, and storage cabinets. All of the facility specifications from the previous task match the requirements for this proposed task. A glass shop with a full-time glass-blower also resides on the first floor of Bldg 23 and provides on-site customized cells with specialized glass to metal seals for our research. The following sections describe the details of the experimental apparatus used in Building 23 during this task.

3.1 Laser Scatter in Microplasma Experiment

3.1.1 *Direct Current Plasma Jet*

The plasma jet device developed for these experiments, shown in Figure 1, is adapted from a design employed by Dudek and Bibinov [28, 29]. The body of the jet device consists of a Teflon base attached to a conical copper shell, which forms the cathode. A sharp tipped steel rod, which forms the anode, extends along the interior centerline of the device, up to a distance of 1 mm from the front exit of the shell. This exit orifice is 2 mm in diameter. The discharge is ignited between the anode tip and the orifice of the cathode shell, which is set at a distance of 1 mm for all experiments. Nitrogen gas is injected into the side of the Teflon tube and flows through the device interior, between the electrode gap and out the front orifice. The plasma jet is formed by the afterglow of the discharge which is carried out of the orifice by the flowing gas. This afterglow is composed of chemically reactive species produced in the high density glow region and includes atomic species (O, N), electronically excited states ($O_2(a_1)$, $O_2(b)$, $N_2(A)$, $N_2(C)$), singlet oxygen (1O_2), and ozone (O_3) [7].

The plasma formed within the jet device is designed to operate in the D.C. glow regime. A schematic of the electrical circuit is also shown in Figure 1.

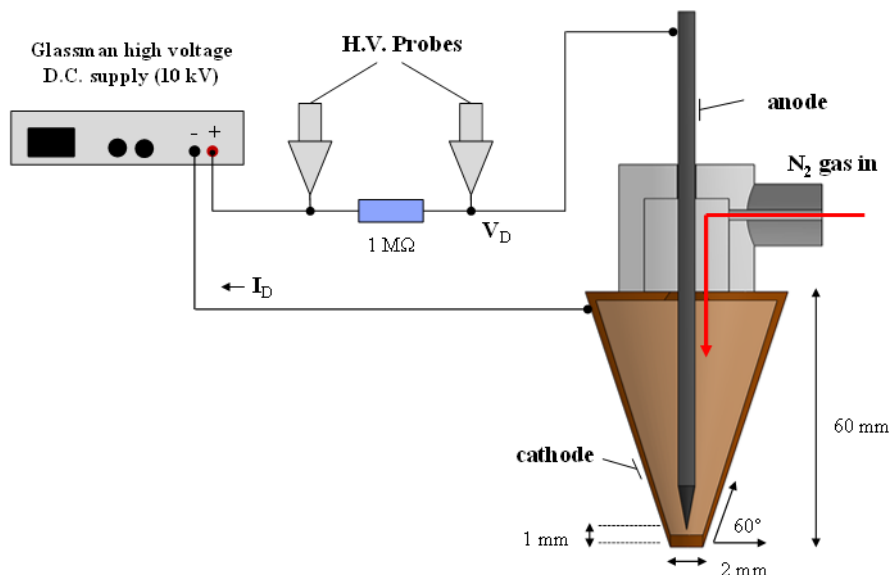


Figure 1: Plasma Jet Body, Integrated into the Accompanying Electrical Circuit
(The high voltage supply excites a D.C. glow between the conical shell (cathode) and the steel tip (anode). The jet is formed by flowing N₂ gas through the plasma discharge, which is emitted through the 2 mm orifice.)

The plasma is initiated using a Glassman high voltage D.C. power supply, capable of voltages up to 10 kV. A ballast resistor (1 MΩ) is placed in series with the plasma to moderate the discharge current. The gap voltage and discharge current were measured using two high voltage probes. A stable operating point for all experiments was chosen to be 375 V and 8 mA. At this condition, a plasma jet extending up to 8 mm visibly out of the orifice was achieved at a nitrogen flow rate of 1.3 standard cubic liters per minute (slm). A photo of the jet operating at this condition is shown in Figure 2. Emission from the plasma can be separated into two regions (1) the active glow, which is concentrated near the electrodes at the jet orifice and (2) the afterglow, which is distributed throughout the downstream jet. Emission in the active glow is due to the production of metastable N₂, which undergoes a variety of transitions, including the second positive system, N₂(C→B) ($\lambda = 300\text{--}450\text{ nm}$), the first negative system, N₂⁺(B→X) ($\lambda = 350\text{--}450\text{ nm}$), and first positive system, N₂(B→A) ($\lambda = 500\text{--}800\text{ nm}$). Emission in the afterglow also originates from metastable N₂, which in this case is transported downstream from its formation in the active glow [7]. Metastable species can alternatively form in the afterglow by way of atomic nitrogen, which has been measured in substantial quantities by Bibinov and Dudek [28]. Atomic nitrogen undergoes three recombination to form the metastable N₂(A) and further leads to N₂(C) through the so called pooling reaction, N₂(A) + N₂(A) → N₂(C) + N₂ [29].

In a typical plasma jet design, it is essential to optimize production of chemical species while minimizing gas heating. Thus, a key component of the design process is reliable measurements of component temperatures in the plasma jet volume. Obtaining spatial resolution within the jet also provides vital information about species production and gas flow parameters. For example, it is known that the transition from laminar flow to turbulent flow out of the orifice may give rise to a dramatic change in gas temperature in the jet [30]. It is conceivable that this also changes the lifetime and path of the chemical species as they travel in the jet. It remains to be seen how gas flow influences species production. The relationship between flow parameters and temperature will be discussed further in Section 4.1.

3.1.2 Glow Discharge Setup

A more conventional atmospheric D.C. discharge was developed for comparison with the plasma jet. The discharge geometry, shown in Figure 3, consists of a pin-pin electrode type, similar to that used by Adams et al. [31]. The anode is composed of a 0.28 mm tungsten wire while the cathode is a formed from a thicker tungsten rod, with radius of curvature 2.0 mm at the tip. Each electrode is attached to an insulating mount, which is positioned on its own translation stage. In all experiments, the electrode gap was set to 2.0 mm.

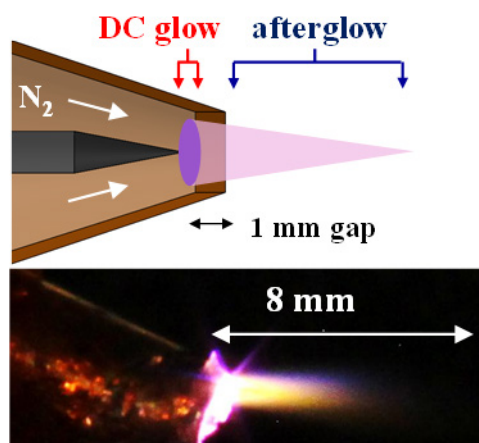


Figure 2: Diagram and Image of the Plasma Jet

(The observed emission is due to optical transitions of metastable N_2 present in the jet.)

The D.C. discharge was initiated using the same electrical circuit used for the plasma jet, as shown in Figure 1. In the D.C. glow setup, the anode tip and cathode shell were replaced by the two respective pin electrodes. Figure 2 shows the orientation used for laser scattering in the glow discharge. As in the case of the plasma jet, the laser path travels downward along the y axis, traveling through the volume of the glow discharge. The laser pathway intersects the electrode axis halfway between the electrodes (1.0 mm from either side), resulting in a laser-plasma interaction zone occurring in the positive column of the glow discharge.

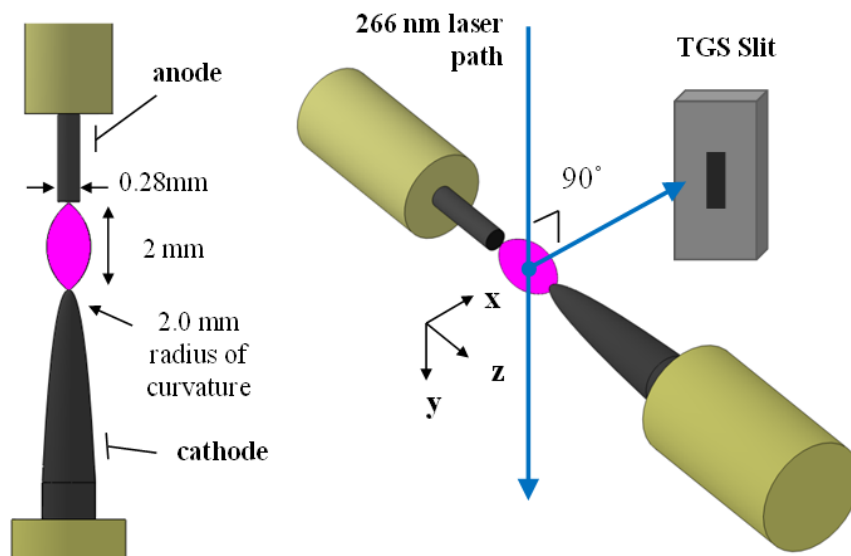


Figure 3: Diagram of the D.C. Glow Discharge Setup

(The D.C. glow discharge setup uses the same electrical circuit shown in Figure 2. A D.C. glow is excited in the 2.0 mm gap of the pin-pin electrode setup. The laser is passed through the discharge (radially) with the same orientation as the plasma jet.)

3.1.3 Laser Scatter Techniques

In plasma diagnostics, there are three different types of laser interactions of interest, Rayleigh scattering, Raman scattering, and Thomson scattering. In Rayleigh scattering, the photon scatters elastically with a molecule, reproducing a photon at the original laser wavelength. This interaction can be used to determine the gas temperature (T_g) of the molecular species. In Raman scattering, by contrast, the photon induces a transition among the rotational energy levels of the molecule, resulting in a scattered photon undergoing a small shift in wavelength. This interaction can be used to determine the rotational temperature (T_r) of the molecular species.

Finally, in Thomson scattering, the photon scatters elastically with a free plasma electron. The elevated temperature of the electron distribution produces a Doppler broadened photon distribution, which can be used to determine the electron temperature (T_e) and electron density (n_e) in the plasma [6]. In this work, laser scattering is restricted to Rayleigh and Raman scattering, which are used to obtain spatially resolved measurements of T_r and T_g in the two plasma sources outlined in Sections 3.1.1 and 3.1.2.

3.1.4 Triple Grating Spectrometer

The scattered laser spectrum can be analyzed using a triple grating spectrometer (TGS), which is required to suppress the dominant Rayleigh peak and extract the low intensity Raman and Thomson signals [32]. Triple grating spectrometers have been employed to investigate a range of laser scattering applications, including Raman scattering [5], Rayleigh scattering [33] and Thomson scattering, [34-36].

Figure 4 shows the basic design of a triple grating spectrometer system. Incident light passing through the first spectrometer is dispersed onto a thin mask, which is positioned to block only the light at the laser wavelength. This light consists of both Rayleigh scatter photons as well as unwanted stray light. The second spectrometer is identical to the first except that the grating is

reversed, causing the dispersed light to be recollected into its original form. The overall effect of this configuration is to remove the strong central peak while preserving the remaining spectral information. Finally, the third spectrometer images the modified spectrum onto an ICCD (Andor DH712 iStar). For this application, the grating density of the third spectrometer was set at 3600 grooves mm^{-1} , which is suited for light in the UV region and is particularly useful for resolving the structure of the Raman spectra. The first two spectrometers were set to a grating density of 1800 grooves mm^{-1} .

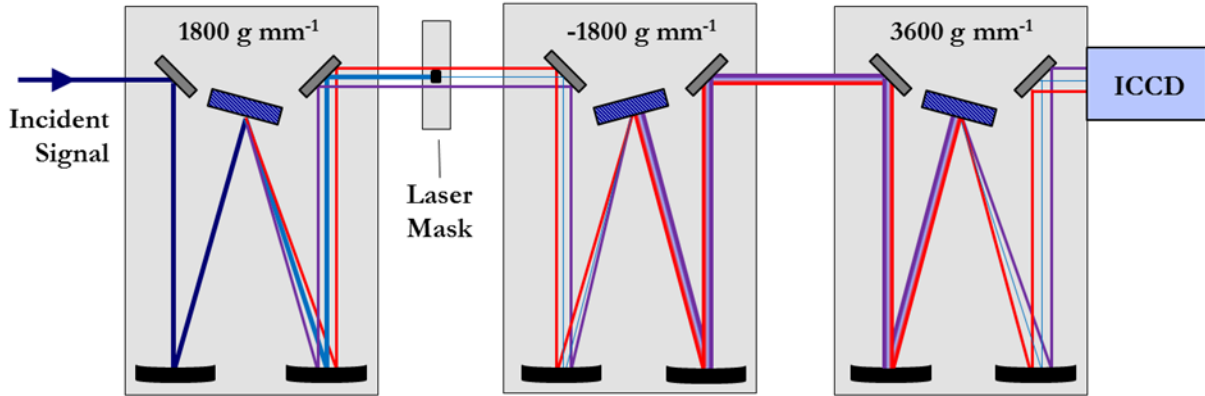


Figure 4: Light Incident on the TGS Entrance

(Light is dispersed by the first grating and imaged onto a 150 μm laser mask, which blocks light at the central 266 nm peak. The second grating recollects the light and images it onto the entrance of the third spectrometer, which disperses the light onto an ICCD similar to a conventional spectrometer.)

The width of the laser mask was designed to block the full Rayleigh peak without removing the usable Raman peaks, which were shifted slightly to either side. The Rayleigh line width is primarily determined by the entrance width of the spectrometer. For all experiments, the entrance slit was set to 150 μm , resulting in a line width of ± 20 pm. The optimal laser mask width was determined to be 150 μm . For a grating density of 1800 grooves mm^{-1} , the bandwidth blocked by this mask is ± 60 pm. If the laser mask is removed, the TGS can then be used to measure the strong Rayleigh signal, which provides the gas temperature, T_g .

3.1.5 Optical Setup

The laser source is a 40 mJ Nd:Yag laser, Q-switched at 10 Hz and frequency quadrupled to produce radiation at 266 nm. Figure 5 shows a diagram of the optical setup used to guide the laser to the plasma and image it onto the TGS system. The 6 mm diameter laser pulse is focused down to a beam waist of 80 μm using a UV lens with focal length 270 mm. For these conditions, a Gaussian beam would have a Rayleigh range of 5 mm [37]. In all experiments, the laser plasma interaction length is 1-2 mm, so the laser beam size can be considered to be relatively constant over the entire interaction zone. The laser pulse was 4 ns in duration. For each shot, the ICCD was gated at 50 ns. The ICCD was binned at single pixels, each with a size of 24 μm . The output of the laser was synchronized with the ICCD using a Stanford delay generator.

In Figure 5, the vectors \mathbf{E}_i and \mathbf{E}_s indicate the polarization of the incident and scattered laser beam respectively. The direction and angle (90°) of \mathbf{E}_i is chosen to maximize the cross section of both Rayleigh and Raman scattering [31]. The laser-plasma interaction was imaged onto the TGS slit using a relay lens pair with focal length 100 mm and was demagnified by a factor of 2. The entrance slit of the TGS system was set to 150 μm wide by 4 mm tall. A pair of irises were

placed at two locations in the imaging path to improve the signal quality. Iris 1 (i_1) was placed in front of the focusing lens in order to minimize the amount of stray light reflecting off the plasma source setup and onto the TGS slit.

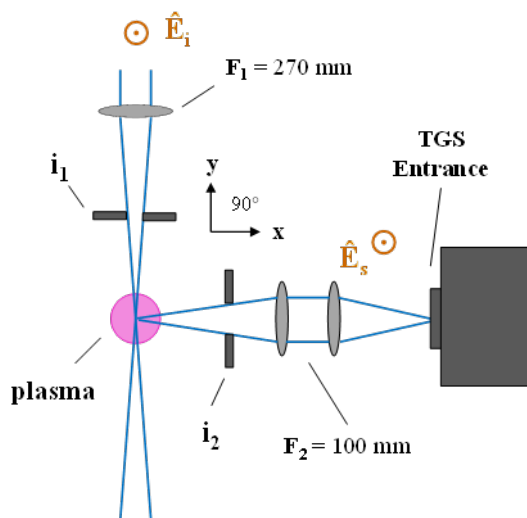


Figure 5: Laser Beam (along \hat{y}) Imaged at 90° onto the TGS Entrance Slit (along \hat{x})
(The plasma jet and D.C. glow electrode axis (along \hat{z}) are both perpendicular to the scatter plane.)

Iris 2 (i_2) was used to control the solid angle of light collection incident on the TGS slit. This allows the collection angle of the relay lens to match that of the spectrometer, thus minimizing the transmission of stray light through the spectrometer [38].

Throughout this report, the following coordinate system is used: the \hat{y} axis is defined to be parallel to the laser path while the \hat{x} axis is defined to be along the imaging path to the spectrometer. By this definition, the \hat{z} -axis is therefore parallel to either the plasma jet centerline (as in Figure 1), or the interelectrode axis of the glow discharge (as in Figure 3).

3.2 Laser Ignition Experiment

A dye laser system with second harmonic generation (SHG) was used to photo-ionize O_2 molecules in laboratory air flow at atmospheric pressure. The second harmonic output of a Nd:YAG laser pumped rhodamine 590 dye to produce a dye laser wavelength of $\lambda = 575$ nm. This was then sent through a SHG crystal, producing a wavelength of $\lambda = 287.5$ nm to match the $O_2(X^3\Sigma)$ to $O_2(C^3\Pi)$ two photon transition wavelength. To allow for variable laser power, the laser was passed through a beam attenuator. The laser was then passed through a lens of focal length $f = 15$ cm and focused through an aperture in the anode and into the center of the interelectrode gap, eventually striking the cathode. The laser focal region extended across the gap with a beam waist of $50\ \mu\text{m}$ and created a continuous channel of high laser energy density between the electrodes. A diagram of the experimental setup of the electrode gap, fuel-air mixture, and high voltage is shown in Figure 1. The laser could be fired with single shots or repetitively at a rate of 10 Hz with energy per pulse variable up to approximately 3 mJ at $\lambda = 287.5$ nm.

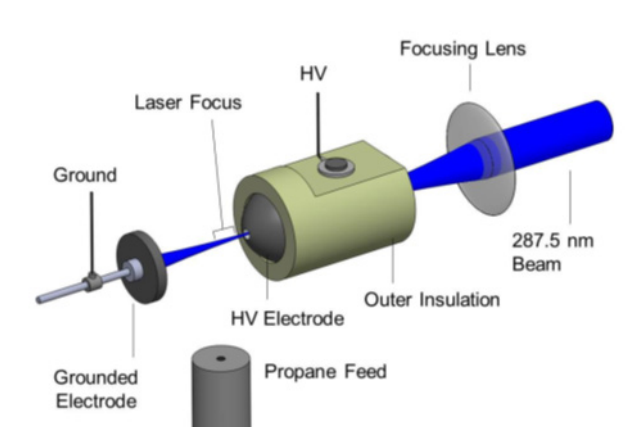


Figure 6: Diagram of Experimental Setup of Laser-induced Ignition Gap

The experimental ignition gap consisted of two electrodes with a 1-mm diameter aperture through in the anode. The anode was fixed in position while the cathode was adjustable to allow for variable interelectrode gap spacing. For our laser induced breakdown technique, the laser beam passed through the anode aperture and was incident on the cathode and any induced arc path generally followed the laser beam path. Near the anode, the arc path branched from the channel of laser photo-ionization to the edge of each electrode aperture.

The high voltage circuit required to energize the ignition gap included a charging circuit consisting of a 100 kV variable DC voltage supply, a 1 M Ω resistor and three 2.2 nF capacitors in series which gave a charging time constant of slightly less than 1 ms. Once charged, the capacitor could be discharged through a circuit that was switched by the ignition arc within the gap. The discharge circuit included a 0.5 M Ω load resistor which limited the discharged current.

A commercial Canon SLR digital camera was used to capture general images of the main arc and any subsequent discharges. The time integration of these photographs was on the order of 0.1 s and thus many of the features in an image could be occurring at various times after the laser pulse. High speed imaging of the laser induced ignition event is conducted with a Phantom v12.0 high speed video camera system with a frame rate of 6,900 frames per second and exposure time of about 150 μ s. Images of the emission from the pre-ionization activity during and shortly after the laser pulse were also captured using an Andor intensified charge-coupled device (ICCD) with an even shorter exposure time of 10 ns. Spectral data were acquired using a fiber optic collection head coupled to an Acton 0.5 spectrometer with an ICCD detector.

3.3 Ion Chemistry of Fuels Experiment

The Fourier Transfer Mass Spectrometer (FTMS) used in the task was originally purchased as a Nicolet FTMS-1000 model and has been upgraded and reconfigured several times over the past two decades. A photograph of the FTMS and data acquisition system in its dedicated laboratory room in Bldg 23 is shown here. The system is based on a 2 Tesla superconducting magnet housed in liquid helium filled chamber.

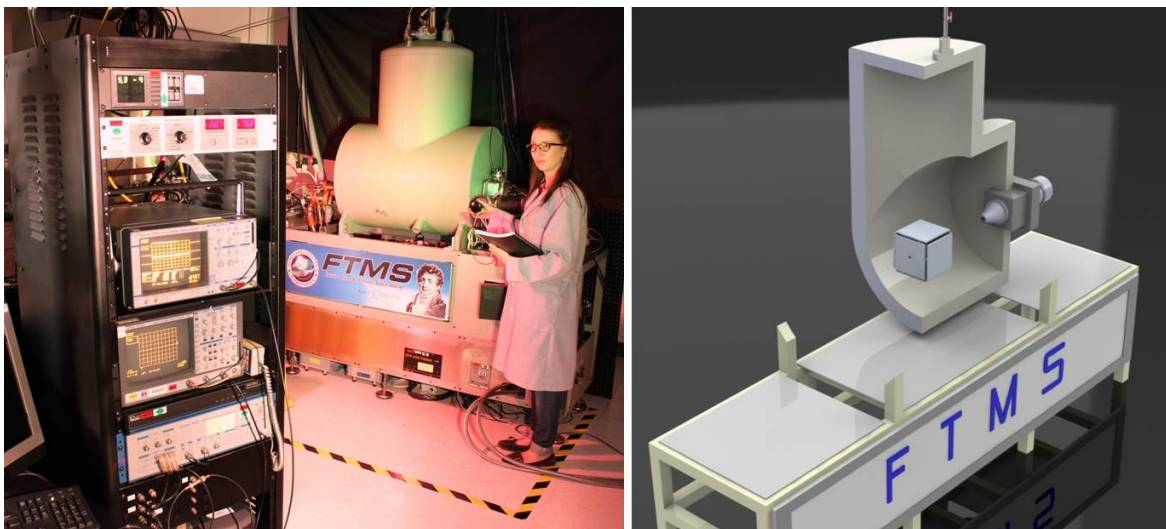


Figure 7: Photograph of FTMS System (left) and Cutaway Showing the Internal Electron Gun and Trapping Cube (right)

Of the original Nicolet apparatus, only the superconducting magnet, gas manifolds and vacuum chamber remain intact. A schematic of the present FTMS apparatus along with its supporting electron gun, ion excitation and detection electronics, data acquisition system, and gas flow and vacuum system is shown in Figure 8.

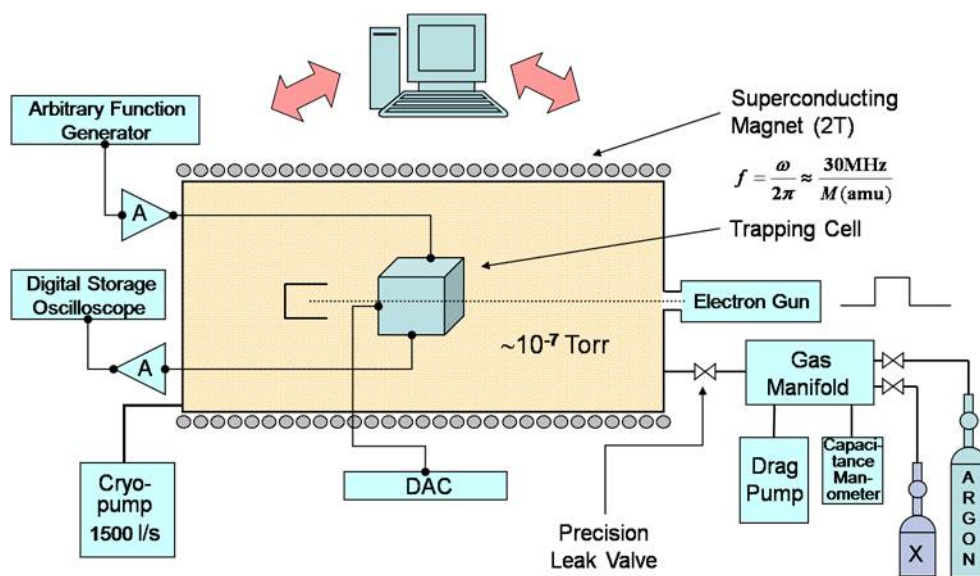


Figure 8: Schematic of FTMS Apparatus for Electron Impact Ionization Studies

In operation, the FTMS directs a pulsed electron beam with a select energy into a cubic trapping cell (5 cm on a side) with a low pressure target gas ($\sim 10^{-7}$ Torr) in the presence of a 2 T magnetic field. The target gas can be a sample gas for analysis or argon for calibration. From the gas manifold at several Torr pressure, the gas is admitted into the FTMS vacuum system through a precision leak valve. The electron beam pulse is typically a few milliseconds, during which a few hundred picocoulombs of electrons irradiate the gas. If the electron beam energy is above the ionization threshold of the target, ions will be generated by electron impact and an applied

voltage to the trapping plates creates a potential well within the trapping cell. After the electron beam pulse, ion fragments of all mass-to-charge ratios are simultaneously and coherently excited into cyclotron orbits using the Stored Waveform Inverse Fourier Transform (SWIFT). After ion excitation and trapping, the ion fragments are detected through image currents on a pair of detection plates integrated within the cubic trapping cell. A Fourier transform of the detection current produces a mass spectrum that can identify the mass number of the ion(s) and indicate the relative ion density by the mass line intensity.

The functions of ion excitation and trapping, ion detection by image currents, and Fourier transform analysis of the ion signal to produce a mass spectrum are illustrated in Figure 9.

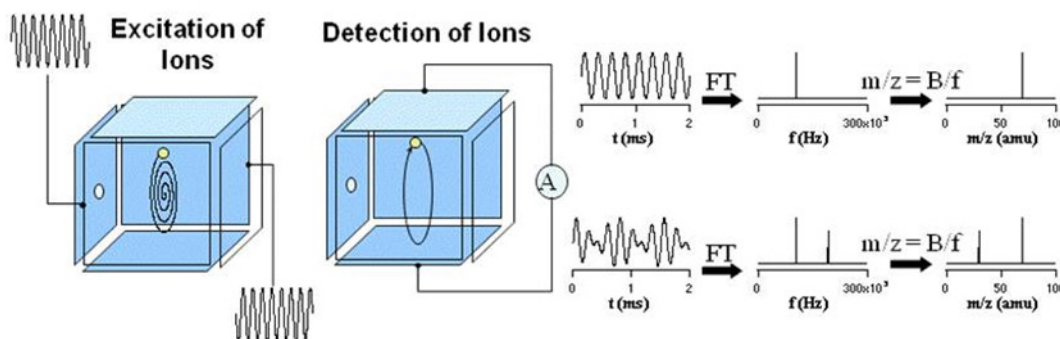


Figure 9: Functional Diagram of Ion Excitation and Detection with Example Ion Signals

The ion trapping cell has been modified to enhance the trapping performance of the FTMS. The previous design had a standard potential well within the trapping cell that could only collect ions with up to 0.66 eV and had a parabolic shaped potential across the cell allowing ions produced near the edge to possibly escape. The modification included the addition of screen electrodes adjacent to the excitation plates that allow the instrument to collect ions with kinetic energy up to ~10 eV, while at the same time maintaining a small potential drop in most of the volume of the cell space. A diagram of this modified trapping cell is shown in Figure 10.

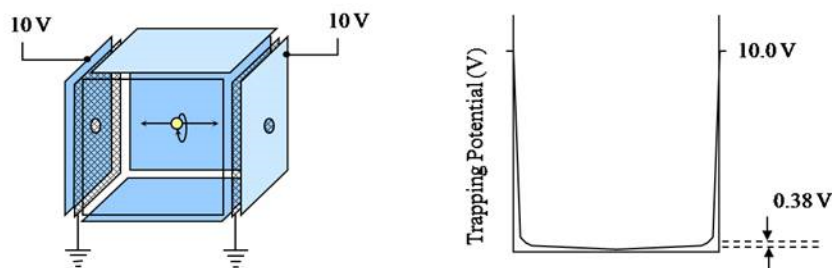


Figure 10: Diagram of Modified Ion Trapping Cell with Screen Electrodes that Trap Ions

The temporal sequence of the FTMS operation is critical to trapping and analyzing the ions created by electron impact. The sequence is shown graphically in Figure 11 with the top trace representing the electron impact ionization of a fresh gas sample, the second trace representing the rf excitation which resonantly excites ions with all mass numbers, the third trace representing the monitoring of the image current signal from the trapped ions and Fourier transforming the signal to determine the ion masses, and the bottom trace representing the large amplitude excitation that removes the ions from the cell and readies it for the next electron beam pulse.

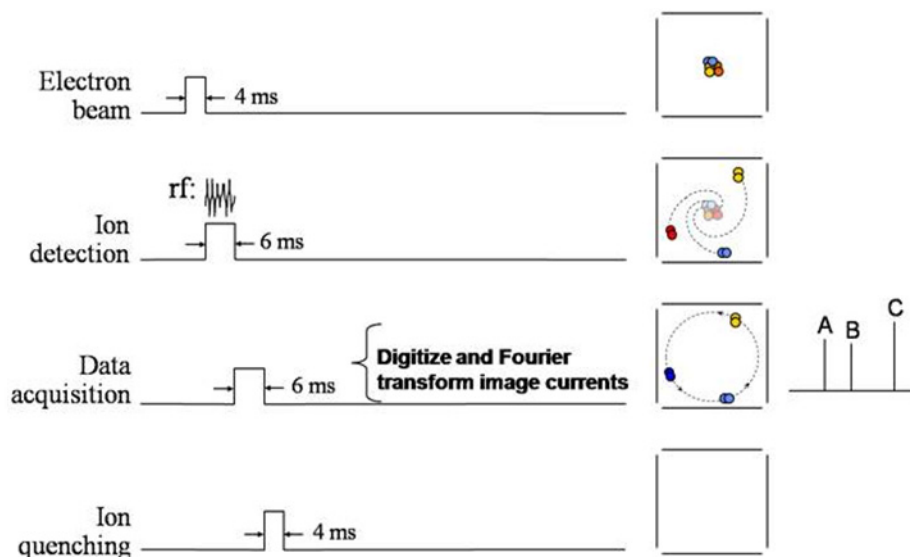


Figure 11: Temporal Sequence of the Ionization and Detection within the FTMS

For a specific electron beam energy, this sequence is repeated at 20 Hz with the digitized image current waveform being average for 10,000 electron beam pulses to produce each mass spectrum for that electron energy. The electron energy of the beam is then changed by a set increment and the averaging process repeated. By varying the electron energy through a large range, a comprehensive set of data can be collected that shows the relative density of all ion fragment masses as a function of electron energy. Each individual ion fragment of a specific mass with a substantial density can then be analyzed for its cross section to be produced from the parent molecule as a function of electron energy. Finally, by calibrating the intensities with an argon sample, the absolute cross section can be found for the ionization of the parent into each specific fragment.

In addition to absolute electron impact ionization cross section measurements, this modified FTMS system is also capable of isolating a single ion fragment and then measuring the subsequent ion plus parent molecule reaction kinetics for that fragment. The sequence for the ion plus parent molecule reaction analysis is shown in Figure 12.

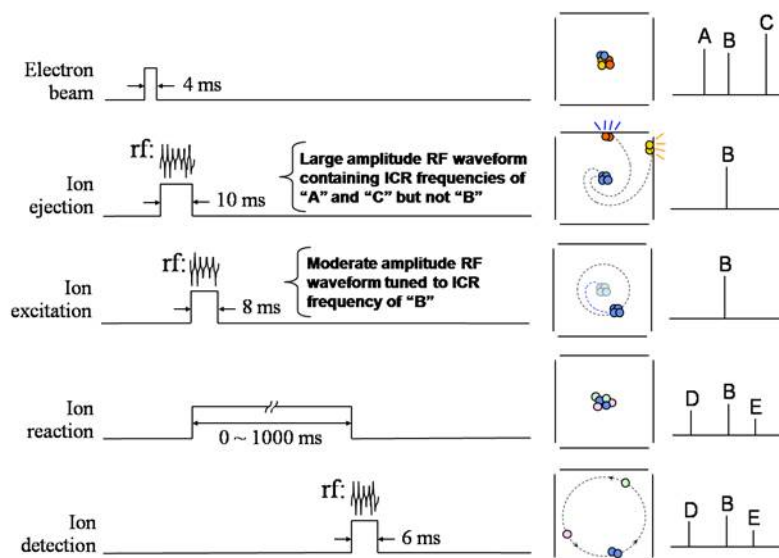


Figure 12: Diagram of Sequence for the Ion Plus Parent Molecule Reaction Analysis

Since the product fragments of the ion plus parent molecule reaction are readily identified in the mass spectra, the resulting reaction rates are specific to the channel generating the product fragment. In Figure 12, the electron beam ionization is again shown in the top trace, in the second trace depicts the SWIFT excitation which rejects ions of all mass numbers (fragments A and C) but not that of the select ion to be studied (B), the third trace then represents rf excitation of the select ion (B) into a trapped cyclotron orbit within the cell, the fourth trace is a delay period in which ion-molecule reactions are allowed to proceed, and the fifth trace represents both the SWIFT excitation of ions with all mass numbers and the image current detection resulting in the Fourier transform mass spectrum of all the product ions created during that reaction period (D and E). An optional step can be taking to heat the specific ion fragments to be studied before the ion plus parent molecule reaction to determine the temperature dependent reaction rates.

All of the experiments were performed using a modified FTMS equipped with a cubic ion cyclotron resonance trapping cell (5 cm on a side) and a 2 T superconducting magnet [39]. For the electron ionization cross section measurements, triethylborane (TEB) (95+%, Sigma-Aldrich) was mixed with Ar (99.999%, Matheson) in a pressure ratio of ~1:1 to a total pressure of ~25 Torr, as determined by capacitance manometry. The mixture was then admitted through a precision leak valve (Varian variable leak valve) into the FTMS system. Ions were formed by electron impact in the trapping cell at pressures in the 10^{-7} Torr range. An electron gun (Kimball Physics ELG-2A, Wilton, NH) irradiated the cell with a few hundred picocoulombs of electrons at a varying energy within the range of 6.6-200 eV, with a spectral width of ± 0.6 eV. The motions of the product ions were constrained radially by the superconducting magnetic field and axially by an electrostatic potential applied to the faces of the cubic trapping cell that were perpendicular to the magnetic field. Ions of all mass-to-charge ratios, in a range of 10 to 500 amu, were simultaneously and coherently excited into cyclotron orbits by applying a Stored Waveform Inverse Fourier Transform (SWIFT) [40] to two opposing trap faces that were parallel to the magnetic field. Following cyclotron excitation, the image currents induced on the two remaining faces of the trap were amplified, digitized and Fourier analyzed to yield a mass spectrum. In this study, the intensity ratios of the ions from TEB to Ar^+ gave cross sections

relative to those for electron ionization of Ar, [41] since the pressure ratio of TEB to Ar was known.

The pressure ratio of TEB to Ar in the trapping cell region mentioned above is assigned to be equal to the pressure ratio in the manifold, based on the following reasoning. Given the pressures in the manifold and the trapping cell region, the leak valve opening, i.e., the gap between the sapphire and the metal gasket, is estimated to be on the order of submicron. The gap is therefore smaller than the mean free path of atoms/molecules in the manifold, which is on the order of a micron, and therefore diffusion of the gas through the leak valve is characterized by molecular flow, which is proportional to $P_m M^{-0.5}$, where P_m is the manifold pressure and M the species atomic/molecular mass. At the low pressures in the trapping cell region, flow to the cryopump (1500 l/s) is likewise molecular with a conductance of approximately 65 l/s through the connecting vacuum lines. Therefore the pump rate out of the trapping cell is proportional to $P_t M^{-0.5}$, where P_t is the pressure in the trapping cell. In summary, at equilibrium P_t depends on P_m and the leak valve aperture but not M because both in-flow and out-flow are diffusive and the atomic/molecular mass effect is cancelled out. The absence of mass discrimination in the pressure ratio of the trapping cell region is confirmed by experiments in which a mixture of Ar and Xe gases is used and the measured ion intensity ratio is compared to the known ionization cross sections of these gases [42]. A typical experiment is finished during a timeframe in which there is no significant pressure change in the manifold so that the pressure ratio is constant.

Due to the limits of electronic parameters used in the current FTMS system that set the lower mass limit at 10 amu, H^+ is not detectable in our experiments. The partial ionization cross section of H^+ is expected to be negligible; however, this ion is absent in the mass spectrum of TEB made by the NIST measurement that allows H^+ to be detected [43].

To study the reactions between ions from TEB electron ionization and the parent molecule, a mixture of TEB and Ar with a pressure ratio of $\sim 1:20$ was used. The ion to be studied was selected by using SWIFT to eject other ions out of the trapping cell, followed by a cooling period in which the ion underwent collisions with Ar at a total pressure of $\sim 1 \times 10^{-5}$ Torr for various times, typically 500 ms. SWIFT was used again to select the ion to be studied from others that were formed during the cooling period, followed by a programmed reaction time selectable typically from 0 to 2000 ms. The pressure of Ar and the length of the cooling period were adjusted so that at the end of the cooling period there were still sufficient reactant ions to study and their reaction showed a single exponential decay to the end of the reaction time at which only a few percent of the reactant ions were left over. With the high Ar partial pressure, Ar^+ was overpopulated during the normal electron ionization procedure, resulting in a significant space charge effect. To eliminate this effect, an RF waveform with the appropriate single-frequency for Ar^+ cyclotron resonance was applied during the electron beam event to continuously and selectively eject Ar^+ out of the trapping cell, for the purpose to reduce the Ar^+ population in the trapping cell.

4 RESULTS

4.1 Laser Scatter in Microplasma Results

4.1.1 Rayleigh Scattering

The gas kinetic temperature, T_g , in the plasma can be calculated using the relations for the scattered Rayleigh intensity, I_{ray} and the gas pressure p_0 ,

$$I_{ray} = I_0 N_g \sigma_{Ray} L \quad (1a)$$

$$p_0 = N_g k_B T_g \quad (1b)$$

In Equation 1a, the scattering intensity is proportional to the molecular density, N_g , the incident laser intensity, I_0 , the interaction length, L , and the Rayleigh scattering cross section, σ_{Ray} . If the plasma is assumed to be a constant pressure ideal gas, then the product $N_g T_g$ remains constant. Hence, the scattered intensity, I_{ray} , (which is proportional to N_g) scales inversely with the gas temperature T_g . The plasma gas temperature can be computed by comparing the scatter signal with the plasma on, I_{on} , to the scatter signal with the plasma off, I_{off} . Figure 13 shows an example of the Rayleigh scatter images taken with the plasma off (left) and with the plasma on (right).

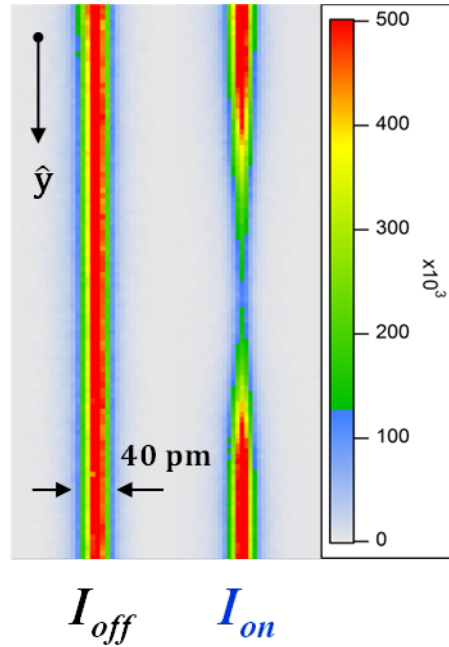


Figure 13: Obtained Gas Temperature T_g

(T_g is obtained by comparing the 1D scatter profile with the plasma on (I_{on}) to that with the plasma off (I_{off}). To the right of these images is the scale for scatter intensity.)

When the plasma is on, the reduction in density, which accompanies the increase in temperature, leads to a reduction in the scatter intensity. Equations 1a and 1b can be combined to obtain the position dependent gas temperature, $T_g(y)$,

$$T_g(y) = \frac{I_{off}(y)}{I_{on}(y)} T_0 \quad (2)$$

Here T_0 is a reference temperature taken with the plasma off, in this case 300 K. Equation 2 can be used to produce a 1D profile of T_g . An example is shown in Figure 14. The resolution of each profile is defined as the length of plasma imaged onto a single pixel, which was 50 μm .

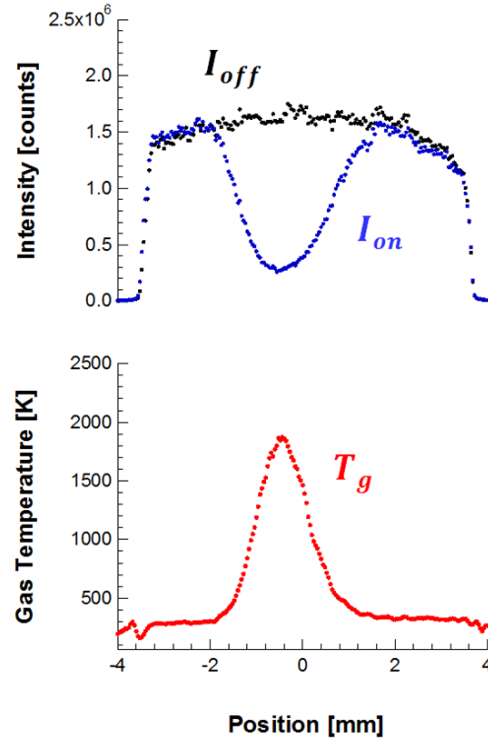


Figure 14: Example 1D T_g Profile

(The 1D T_g profile is calculated along the radial axis of the D.C. glow discharge. The spatial resolution is 50 μm .)

4.1.2 Rotational Raman Scattering

The scatter photon intensity resulting from a Raman transition from a rotational state J to state J' is given by,

$$I_{ram}(J \rightarrow J') = I_0 N_J \sigma_{J \rightarrow J'} L \quad (3)$$

In this equation, I_0 is the incident photon intensity, N_J is the density of species in rotational state, J , and $\sigma_{J \rightarrow J'}$ is the cross section for the $J \rightarrow J'$ transition. The rotational distribution, N_J is determined by the total gas density of the species, N_g , the rotational partition function Z_r , and the rotational temperature, T_r . In thermal equilibrium, the rotational states can be described by a Boltzmann distribution,

$$N_J = \frac{N_g}{Z_r} g_J (2J + 1) \exp\left(-\frac{E_J}{k_B T_r}\right) \quad (4)$$

The factor g_J is the nuclear degeneracy factor, which imparts an extra multiplicity on the total J states depending on whether the rotational state is even or odd. For Nitrogen, g_J is 3 and

6 for odd and even J respectively. Oxygen, in contrast, has values of 1 and 0 for odd and even J , meaning that only states with odd J are present in the spectra [44]. The interaction of laser photons at wavelength, λ_0 , with the rotational states described by (4) gives rise to a discrete spectrum of scattered photons,

$$\lambda_{J \rightarrow J'} = \lambda_0 + \frac{\lambda_0^2}{hc} B \cdot (J'^2 + J' - J^2 - J) \quad (5)$$

This spectrum is further defined by the selection rule, $\Delta J = \pm 2$, which gives rise to the so called Stokes lines ($\Delta J = +2$) occurring at wavelengths above λ_0 , and anti-Stokes lines ($\Delta J = -2$) occurring at wavelengths below λ_0 . Figure 15 shows an example of an experimentally obtained Raman spectra in pure nitrogen gas. As expected, the central Rayleigh peak is suppressed by the TGS laser mask. The Stokes and anti-Stokes bands are observed to the left and right of the laser line. The alternation of the Raman peaks is due to the degeneracy factor, g_J , which alternates between even and odd J .

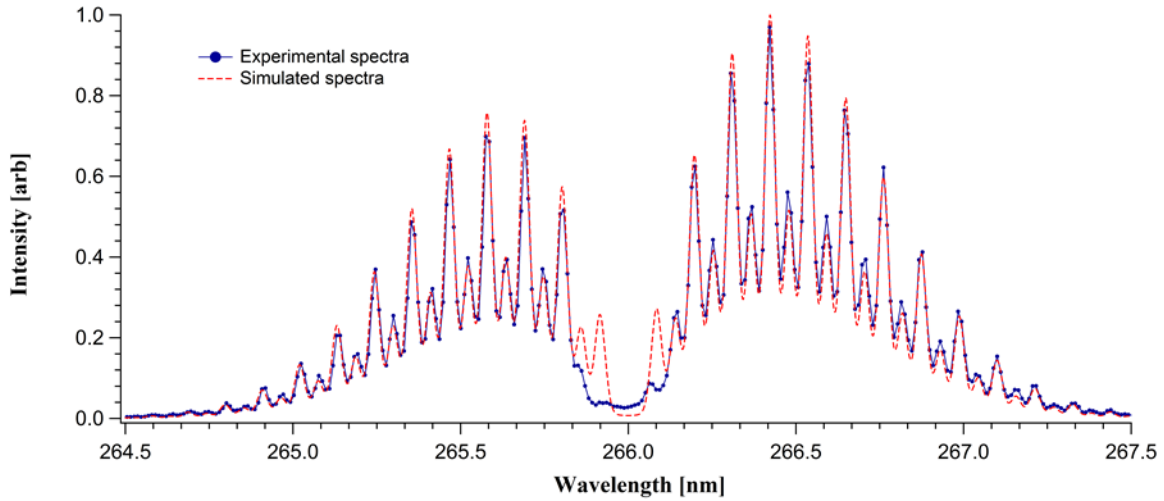


Figure 15: Typical Raman Spectra Taken at a Slit Width of 150 μm

(The Rayleigh peak normally observed at the laser line (266 nm) is blocked by the TGS laser mask. Also shown is a simulation of the Raman spectra under the same conditions.)

For all Raman measurements, the TGS entrance slit width was set to 150 μm with a mask width of 150 μm . As in the case of Rayleigh imaging, the interaction zone was imaged vertically parallel to the slit. In order to improve the signal strength, the ICCD was binned vertically over 8 pixels, corresponding to 150 μm of the plasma. This distance forms the spatial resolution of Raman images.

Accompanying the nitrogen Raman data in Figure 15 is a computational simulation of the Raman spectra using a program developed with IGOR Pro software. The program is designed to calculate the expected Raman transition lines, populate the scattered intensity distribution for a given rotational temperature, T_r , and then apply a broadening mechanism that is determined by the spectrometer instrument profile. The instrument profile is derived from a number of broadening mechanisms, including optical aberrations, diffraction gratings, and the spectrometer entrance slit width. The program was used to calculate the rotational temperature of experimental spectra, such as the one shown in Figure 15. For each spectra, T_r was determined using a method similar to a least squares fit, in which the square of the pointwise difference between simulation and experiment was minimized over a range of T_r . The entire process of T_r measurement was

calibrated using a glass cell containing nitrogen gas. The gas in the cell was heated to a series of temperatures as measured using thermocouples. At each point, the rotational temperature was calculated using the fitting program.

4.1.3 Temperature Measurements in the Plasma Jet

Measurements of the gas kinetic temperature were taken in the volume of the plasma jet afterglow occurring outside the jet orifice. First, spatially resolved measurements of T_g were obtained by placing the plasma jet body on a 3D translation stage and moving it through the laser interaction zone. As described in section 3.1 and 3.2, the imaging of the laser interaction zone vertically onto the TGS slit allows 1D spatial profiles to be measured in a single accumulation. However, in order to obtain improved signal to noise level, the scattering signal was accumulated over 3000 laser shots (corresponding to 300 sec) at each position.

Figure 16 shows a 2D map of T_g obtained using Rayleigh scattering. The map was constructed by combining a series of 1D profiles each taken across the radial cross section of the jet (along \hat{y}), as described in section 3.1. The axial dimension was varied by translating the plasma jet axially along the \hat{z} direction in 0.6 mm increments. The position $z = 0$ corresponds to the orifice opening while the first temperature profile begins at the location $z = 1.2$ mm. As described in section 3.1, the spatial resolution of T_g was 50 μm .

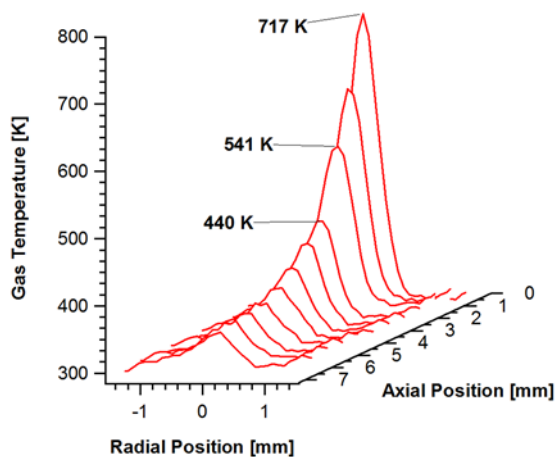


Figure 16: Gas Temperature within the Plasma Jet

(The axial position, $z = 0$, corresponds to the orifice of the device body. The temperature of the jet drops as the gas flows outward and mixes with the ambient air.)

Overall, the 2D map illustrates the spatial variation of gas temperature as the heated gas exits the nozzle and mixes with the ambient air.

The temperature of the jet reaches 717 K at a distance of 1.2 mm from the orifice and cools to 350 K over a distance of 1 cm. The persistence of high temperatures outside the orifice is consistent with the properties of a laminar jet observed by Mohamed et al [30] in a similar plasma jet setup. In that device, Mohamed observed high gas temperatures outside the jet nozzle at Reynolds numbers up to 320. Above these values, the temperature was observed to collapse down to ambient within 1 mm of the nozzle due to the diffusive mixing associated with turbulent flow. In the current experiment, a gas flow rate of 1.3 slm and plasma diameter of 1 mm yields a Reynolds number of 180. This suggests that the plasma jet is laminar. In this regime, the plasma

jet does not mix with the ambient air as it cools down. Instead, as suggested by Dudek et al., the primary mechanism is thermal conduction between the jet region and the ambient air [29].

Raman spectra were also taken at points within the plasma jet and analyzed with the IGOR program to calculate T_r . Figure 17 shows a comparison of T_g and T_r along two different line profiles of the jet. Figure 17a shows a profile along the centerline of the jet orifice, which extends from 0.6 mm to 6.6 mm while Figure 17b shows a profile across the radial axis of the jet, at an axial distance of 1.2 mm from the jet orifice. A physical representation of the jet is shown to clarify the orientation of each profile.

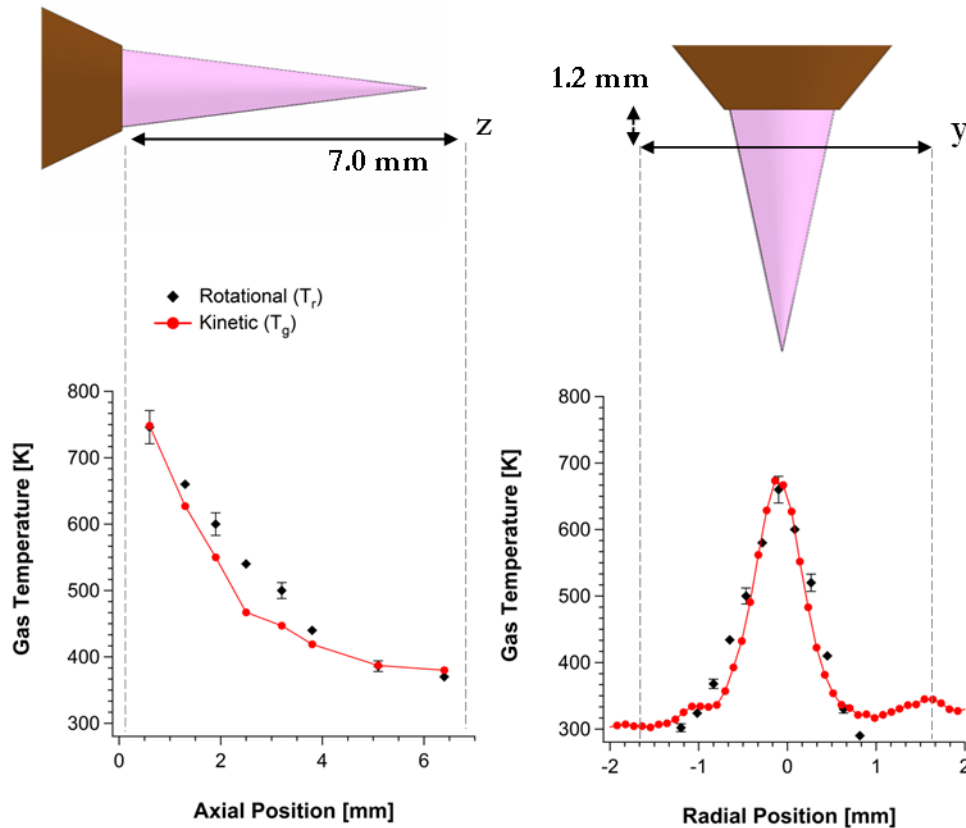


Figure 17: Axial and Radial Temperature Profiles in the Plasma Jet

(The axial profile begins 0.6 mm outside the orifice and extends 6.0 mm out. The radial profile is taken at an axial distance of 1.2 mm. Overall, the two component temperatures (T_g and T_r) agree over the jet region.)

Results from the two profiles indicate that T_r and T_g agree closely over the entire region of the jet. For the axial profile, both temperatures peak at 700-750 K near the orifice and decrease to below 400 K after approximately 6 mm. The radial profile (taken near the orifice) has a full width half maximum of 1 mm, consistent with the dimension of the plasma glow and thus the region over which the gas is heated.

4.1.4 Temperature Measurements in the Glow Discharge

Gas temperature was also measured in the glow discharge, as described in section 1.2. Laser Rayleigh and Raman scattering were used to measure images of T_g and T_r along the \hat{y} axis of the

glow discharge. Figure 18 shows temperature measurements for two different values of discharge current, 4.0 mA and 8.0 mA.

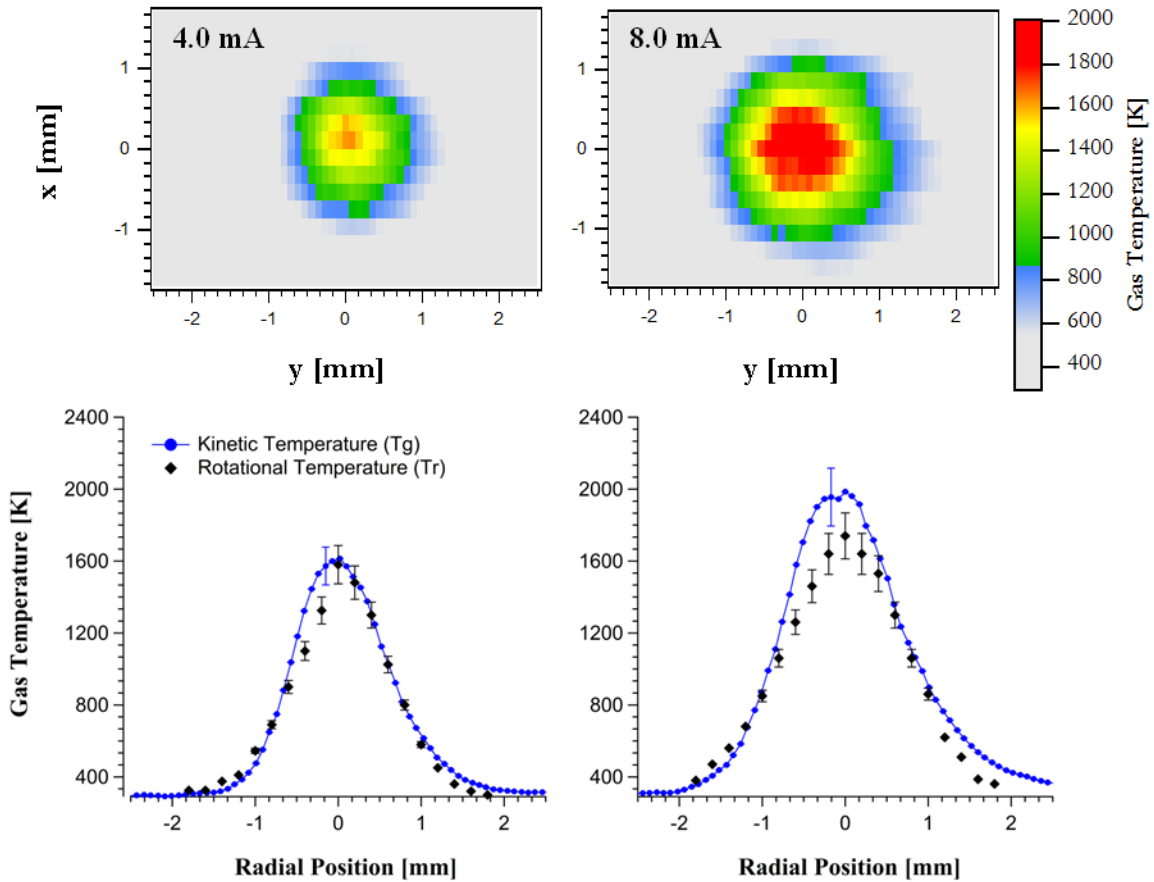


Figure 18: Radial Temperature Profiles Taken in the Pin-pin D.C. Glow Discharge at Two Separate Operating Conditions (left) 4.0 mA and (right) 8.0 mA

(The two component temperatures agree over most of the plasma. The source of disagreement occurs near regions of peak temperature where the measurement uncertainty is largest.)

For each operating condition, a 2D map of T_g was constructed using Rayleigh scattering profiles. This map was generated by a similar procedure to that of the plasma jet map shown in Figure 16. In this case, though, the plasma source was translated in the x direction, perpendicular to the interelectrode axis. The maps represent a radial cross section of the glow discharge taken halfway between the anode and cathode. Below each map is a 1D profile of both temperatures, T_g and T_r , taken through the centerline of the discharge. The measured gas temperatures in the glow discharge (peaking at 2000 K) were considerably higher than those observed in the plasma jet. This is due to the measurements being taken directly in the glow discharge rather than downstream of the nozzle. Comparisons with glow discharges of similar setups show these temperatures to be slightly above previously measured data [31]. The reason for the discrepancy is assumed to be the larger electrode gap (2 mm), which provided less heat transfer by conduction from the plasma to the electrodes than smaller gap configurations. At atmospheric pressure, the electrode gaps are typically spaced under 1 mm in order to minimize breakdown voltage according to Paschen's law. In this work, the larger electrode gap was chosen to minimize stray light resulting from the reflection of laser light off of the electrodes. As a result,

the larger electrode gap required higher power input to sustain the discharge. Future improvements to the spectrometer system will allow electrode gaps under 1 mm, in order to fully investigate the micro discharge regime.

The primary change observed from increasing the discharge current was an increase in both the peak and FWHM of the gas temperature distribution, which is tracked by both diagnostics, T_g and T_r . This behavior is typical of direct current glow discharges, and has been observed using both Rayleigh scattering [31] as well as optical emission spectroscopy in the past. Overall, T_g and T_r agree well over the region of the plasma. In our work however, there was a region where the difference between T_g and T_r was noticeable. This occurred for the condition of highest temperature (the center of the glow discharge at 8.0 mA). This deviation may be due to several possible effects occurring within the high temperature region.

The only significant disagreement between T_g and T_r was observed in regions of peak temperature. The temperature distribution at these high currents appeared to peak over a relatively short distance. The abrupt change in temperature may be a result of the difference in spatial resolution between T_g (50 μm) and T_r (150 μm). This difference might cause the T_r measurements to be spread out over the region of peak temperature, thus lowering the peak T_r .

The disagreement could also originate from the increasingly large uncertainty of T_g at high temperatures, which was due to the low signal-to-noise ratio of the Rayleigh signal. This effect is most significant near regions of peak temperature, particularly for the case of 8 mA discharge current. Similar measurements of a microdischarge in this same setup have estimated the upper temperature limit at 2000 K [31]. Thus, considering the large uncertainty in both the Rayleigh and Raman data in figure 18 at 8 mA, the error bars are very close to overlapping and agreement between T_r and T_g could still be considered legitimate within the uncertainty.

A final possibility for the discrepancy between T_g and T_r is that both measurement sets were accurate and that these components may actually begin to differ slightly within the highest temperature regions of the microdischarge. Because this discrepancy only surfaced at the upper temperature limit of the Rayleigh technique, it could not be pursued further in this experiment, but may be investigated with an improved setup in the future.

4.2 Laser Ignition Results

An example digital camera image is shown in Figure 19, where the exposure time was 0.1 s, which spanned a time period that included the arc event across the laser path, which is clearly seen, as well as the propane ignition and combustion events. The flow was bottom to top in all photographs at a speed of about 10 m/s. Typically the arc is delayed a few hundred nanoseconds after the laser pulse and then the ignition and combustion process progresses over the next several milliseconds. The photograph in Figure 19 captures all these events in one frame.



Figure 19: Digital Camera Image of Laser-induced Ignition

Photographs from the high-speed video camera with an exposure time of 150 ns captured the laser-induced arc before the flame formation. Figure 20 shows examples of the laser-induced arc in air only and air –propane. The air-propane arc displays signs of the hydrocarbon ignition and combustion process starting (greenish blue) that is not present in the air only case.

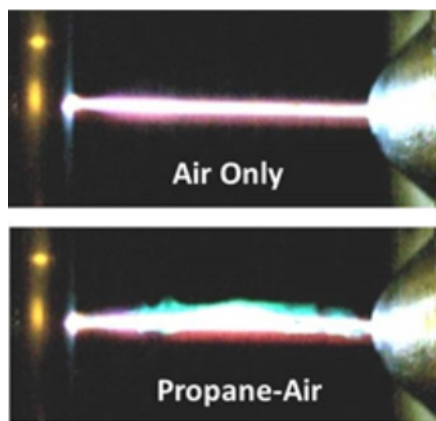


Figure 20: High-speed Images of Laser-induced Arc in Air and Air-propane

The threshold breakdown voltage was determined for the resonant laser-induced ignition technique under various conditions. The plot in Figure 21 shows the dependence of the experimentally measured threshold laser-induced breakdown voltage for various gap spacing and compares this to the well-known standard of $E_b=30$ kV/cm for self-breakdown across a planar gap with either air or a air-propane mixture. The trend in Figure 21 for laser-induced breakdown across gaps of $d = 1$ -5 cm shows that the threshold is about 1/3 of the standard self-breakdown, or about $E_b=10$ kV/cm. The threshold voltage for air-propane was slightly lower than that for air only at all gaps. At gaps of $d = 3$ cm and less, laser-induced arcing was easily achieved with laser energy below 1 mJ. With increasing electric field, our experimental setup with the continuous voltage supply was susceptible to corona discharges and edge arcing which limited the testing of lower laser energies with the larger gap spacing.

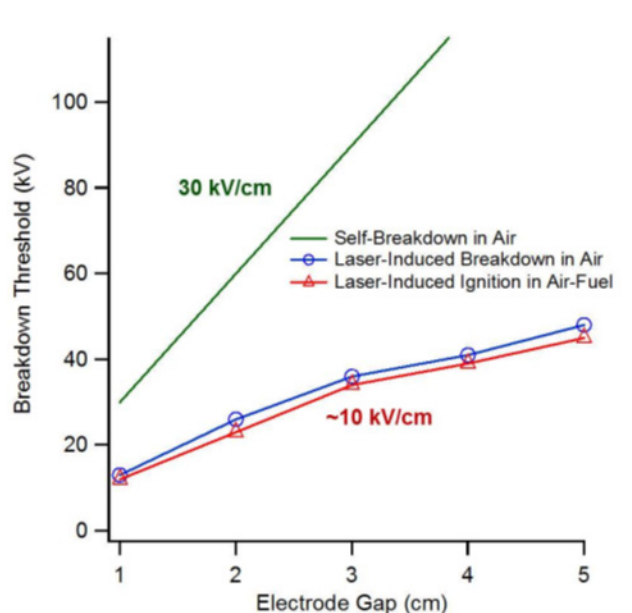


Figure 21: Plot of Breakdown Voltage Threshold

(The breakdown is for various electrode gaps for both air and air-propane compared to the theoretical self-breakdown threshold.)

The emission during the arc delay period was also investigated by imaging and spectroscopy. The results for an air-propane flow through a 2.5 cm gap with 36 kV applied is shown in Figure 22. The image exposures were the shortest yet at 10 ns. During the laser pulse, or 0 ns delay, the emission is seen to be concentrated at the laser focus where most of the REMPI was taking place. The spectrum of the emission reveals that the typical $N_2^+(B-X)$ feature that corresponds to REMPI in atmospheric air is present along with a C_2 emission feature as well. This indicates that the resonant photo-ionization and the applied voltage induced at least some dissociation of the hydrocarbon fuel during this early period. Later images during the delay at 60 ns and 100 ns show mostly $N_2(C-B)$ emission, indicating that direct electron impact was driving the emission, most likely from enhancements in the electric field due to space charge effects along the ionized laser path. The final image at a delay of 140 ns shows emission from the start of the ignition process. The temperature was clearly elevated based on the significant broadening of the molecular emission bands. Also CN emission bands appear in this final image, which indicates a high degree of dissociation and reformation of radicals.

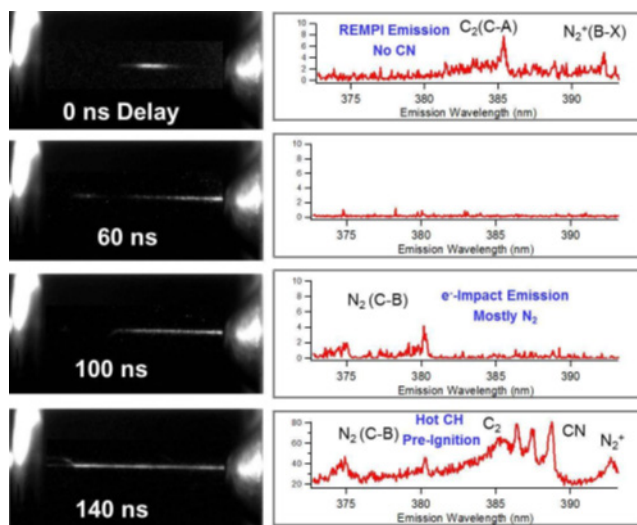
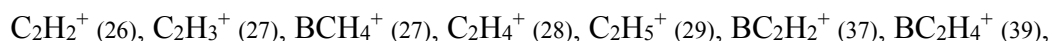


Figure 22: Gated Images and Spectra with 10 ns Resolution
(The images are for various times after the laser pulse for the air-propane case.)

4.3 Ion Chemistry of Fuels Results

4.3.1 Electron Ionization

Two issues cause difficulties in analyzing the mass spectrum of TEB: (a) the two boron isotopes with appreciable natural abundances: boron-11 (^{11}B , 80.1%) and boron-10 (^{10}B , 19.9%), and (b) the possible isobaric ions due to the boron-containing species and non-boron-containing species. For example, at m/z 27, there can be three possible ions: C_2H_3^+ , $^{11}\text{BCH}_4^+$ and $^{10}\text{BCH}_5^+$, with exact masses of 27.0229, 27.0401 and 27.0515 amu, respectively. These isobaric ions often make qualitative and quantitative determination of species difficult. In a mass spectrometry study on boron chemistry a few decade ago, a technique of isotopic variation of the two boron isotopes was used to deduce numbers of boron atoms in particular ions [46]. When the isobaric ions (the boron-containing and non-boron-containing species) overlap, however, this technique will be difficult to implement to determine the accurate distribution of boron isotopes. In this FTMS study on TEB, by means of the high-mass-resolution spectrum to distinguish the isobaric ions, we have identified and quantitatively measured the following ions produced from the electron ionization of TEB, listed in the order of increasing ions mass-to-charge ratio that is shown in the parentheses in the unit of amu:



Certain other ions are observed, but their intensities are rather insignificant to be quantitatively measurable. The ion mass shown above in parentheses assumes any boron is the main isotope ^{11}B , but when assigning the ion identities and ion intensities used to derive partial ionization cross sections (see below), B in the formulae then represents both isotopes of boron. The same issue also applies for C (^{12}C and ^{13}C). This implication applies elsewhere in the text unless a specific isotope is indicated. By exact mass measurements, the existence in any significant amount of many possible isobaric ions from TEB has been ruled out. For example, in the region of m/z 26 as shown in Figure 23, there are only C_2H_2^+ and $^{10}\text{BCH}_4^+$; $^{11}\text{BCH}_3^+$ is

negligible. In the regions of m/z 28 and 29, there are only $C_2H_4^+$ and $C_2H_5^+$, respectively, and $^{11}BCH_5^+$ and $^{11}BCH_6^+$ are absent, respectively. The absence of these boron-carbon species will be discussed later. At m/z 68 there is mostly $^{10}BC_4H_{10}^+$, with a minor amount of $^{11}BC_4H_9^+$. As seen from the above list, there is only one pair of isobaric ions: $C_2H_3^+$ and BCH_4^+ at m/z 27, and there appears to be a trend: heavy ions are exclusively boron-carbon species, while the light ions are essentially non-boron-containing species, with a boron-containing isobaric ion at m/z 27. The absence of large non-boron-containing ions seems to indicate that, during the fragmentation of the parent ion, no new C-C bond is formed to produce hydrocarbon ions larger than $C_2H_5^+$.

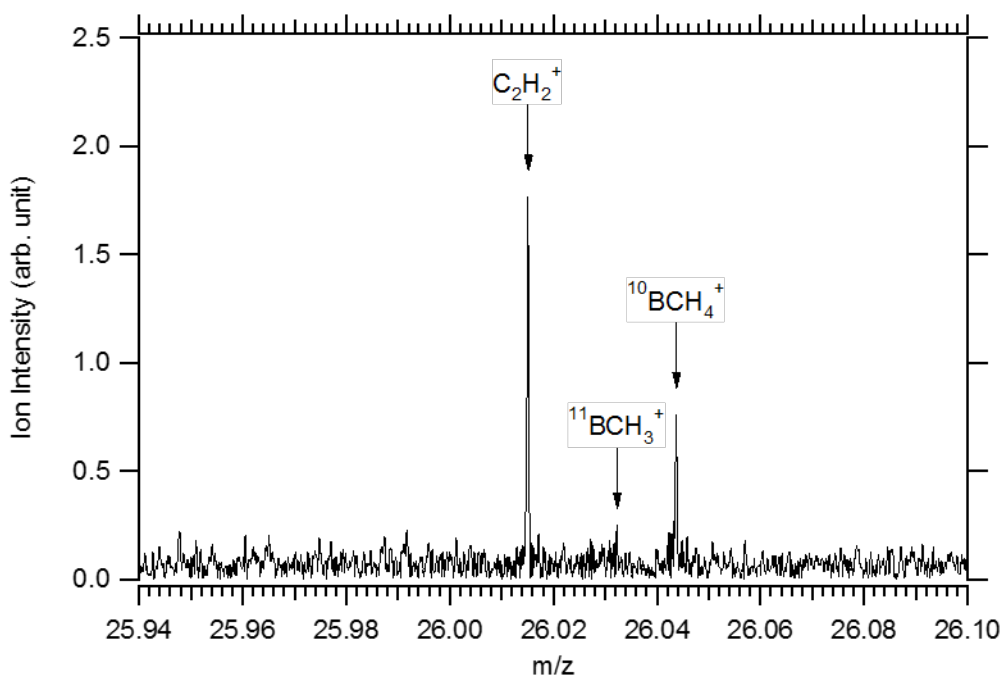


Figure 23: A High-resolution Mass Spectrum at m/z 26 Showing Multiple Isobaric Ions

No noteworthy doubly-charged ions are observed, but the possible ones that have the same mass-to-charge ratios as the singly charged ions listed above cannot be excluded; these doubly and singly charged ions having the same mass-to-charge ratios are not distinguishable by mass spectrometry methods. Certain amounts of the singly charged ions listed above may be formed by dissociative double ionization and thus carry significant amounts of kinetic energy. In our experiments, as described in more details previously [47], with a pair of screen electrodes and 10 V trapping potential, we expect to be able to trap most of the energetic ions with energies up to a few eV. For example, 97% of the ions with 5 eV kinetic energy are expected to be detected. Since the energetic ions are of minor population, a missing few percent of the energetic ions should not severely affect the measurement of the total cross section within its error margins.

The total and partial electron ionization cross sections as functions of the electron energy in a range from 6.6 to 200 eV are shown in Figures 24 and 25. The peak of the total cross section is located in the 65-85 eV region, with a value of $2.2 \times 10^{-15} \text{ cm}^2$. The uncertainty of the cross section data includes $\pm 14\%$ of estimated possible errors in FTMS experiments [48], and an additional $\pm 3.5\%$ for the Ar cross section [41] calibration. As shown in Figure 25, the most abundant ions are the parent ion $BC_6H_{15}^+$ and fragment ions $BC_4H_{10}^+$ and $BC_2H_6^+$; together the three ions account for more than four-fifths of the ion population throughout the energy range studied. The formation of the parent ion has the onset energy at 9.6 eV. At higher energies after

the parent ion onset, the fragment ion $\text{BC}_4\text{H}_{10}^+$ appears, with the onset energy of 9.8 eV, formed by loss of a ligand (C_2H_5 radical) of B in the parent ion, resulting in a valence structure of $(\text{C}_2\text{H}_5)\text{-B}^+(\text{C}_2\text{H}_5)$. At 11.4 eV, the fragment ion BC_2H_6^+ emerges, which is expected to be formed by further dissociation of $\text{BC}_4\text{H}_{10}^+$ via loss of C_2H_4 , with an H atom from a cleaved ethyl group attaching itself to the B atom [46], resulting in a valence structure of $(\text{C}_2\text{H}_5)\text{-B}^+\text{-H}$.

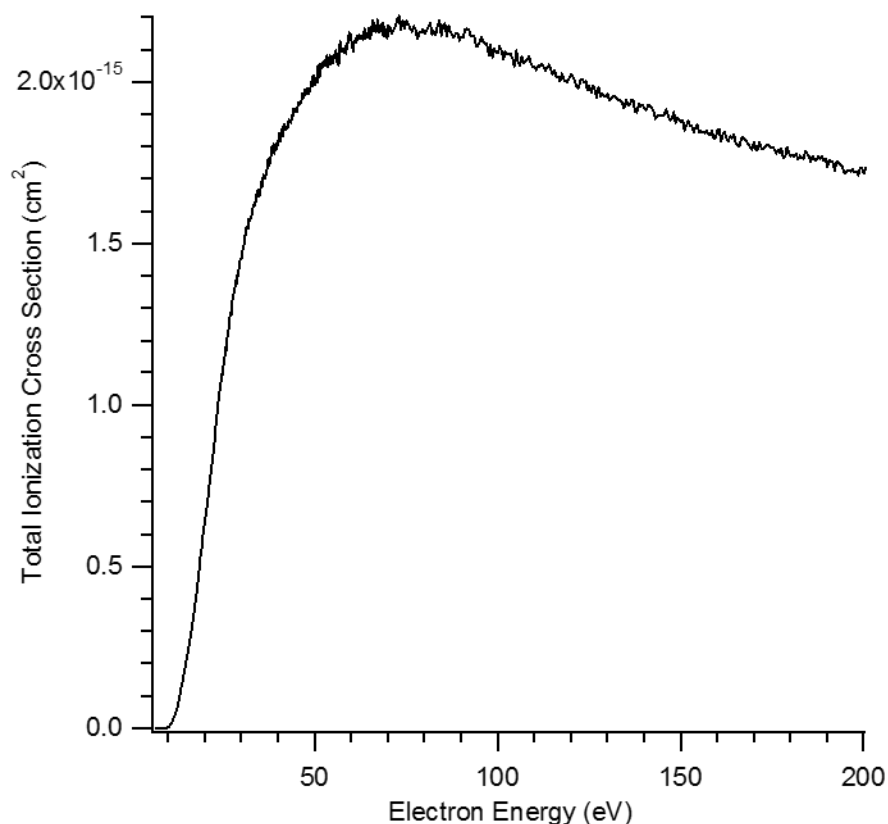


Figure 24: Total Electron Ionization Cross Section of TEB

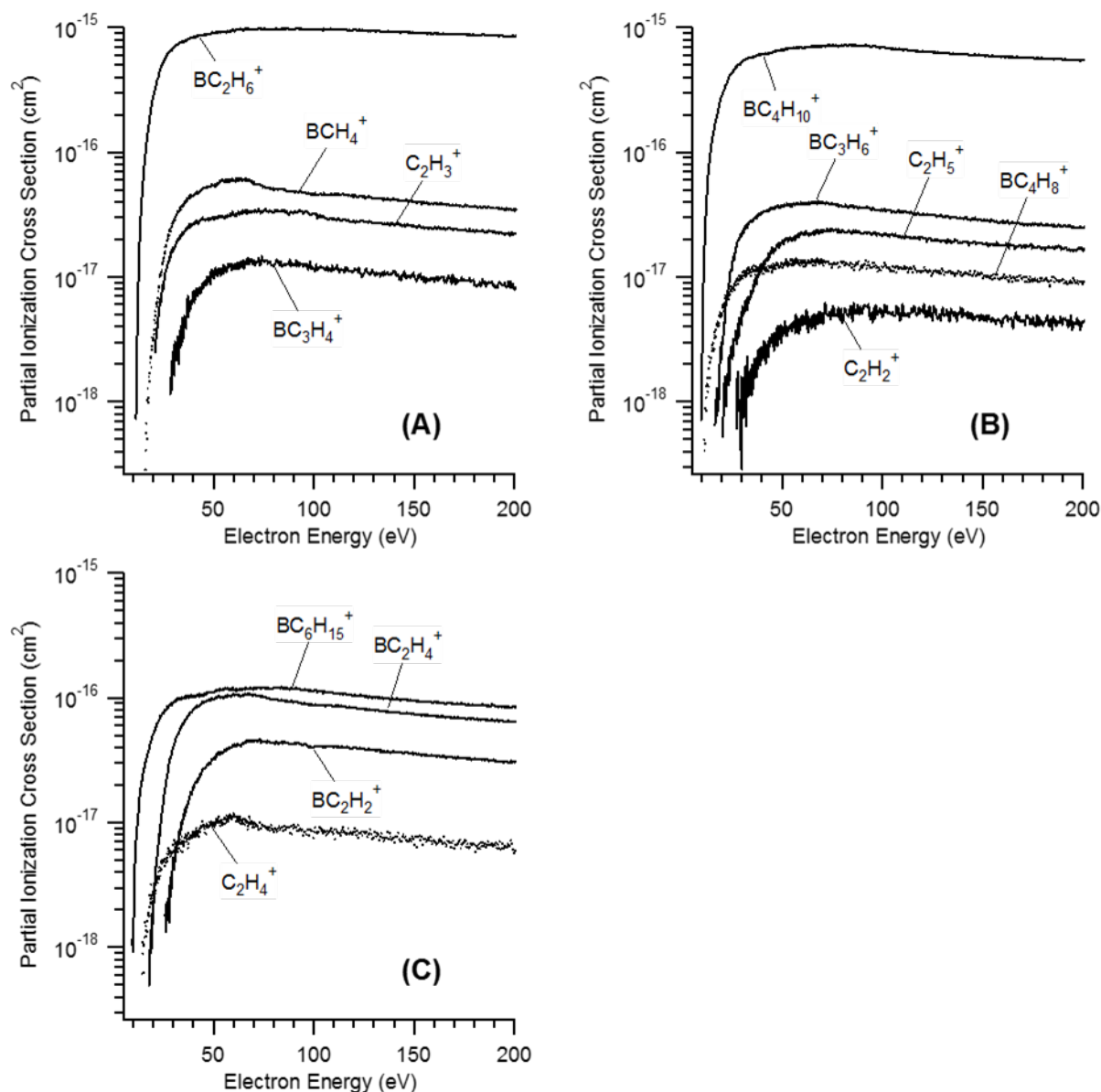


Figure 25: Log plots of Partial Cross Sections for Major Product Ions from Electron Ionization of TEB

(For visual clarity data are presented in three graphs, in which scales are set to the same for easy comparison of the amplitudes for different ionization channels. The display mode of lines-between-points is used, except for certain ions: BCH_4^+ in (a), $BC_4H_8^+$ in (b) and $C_2H_4^+$ in (c), which are presented using dots at points, for the purpose of easy distinguishing data for different ions.)

The valence structures for $BC_4H_{10}^+$ and $BC_2H_6^+$ mentioned above can be attributed to the preferred oxidation number of B: +3; the singly-charged B atom can only bind to two ligands. Based on this argument, we propose the valence structure of BCH_4^+ to be $(CH_3)-B^+-H$, and the absence of BCH_5^+ and BCH_6^+ mentioned earlier can be explained by the fact that the oxidation number of B in the these two ions would exceed +3 in these two hypothetical valence structures, respectively: $[(CH_3)-BH_2]^+$ and $[(CH_3)-BH_3]^+$.

4.3.2 Ion-molecule Reactions

Gas-phase reactions between TEB and certain major ions from the electron ionization of TEB are summarized in Table 1. Also included in the table is the reaction of Ar^+ with TEB. After 70-eV electron ionization to produce the ions, the ion to be studied is isolated and thermalized by collisions with Ar gas under $\sim 1 \times 10^{-5}$ Torr pressure for a certain length of time, typically 500 ms, followed by its reaction with TEB. Listed in table 1 are the reaction rates relative to the Ar^+ reaction, the product ions and their branching ratios. We didn't isolate the two isobaric reactant ions at m/z 27, C_2H_3^+ and BCH_4^+ , because their masses are too close for us to isolate one from the other. Although we can determine the individual decay rate of each isobaric ion to derive its reaction rates, we cannot resolve the product branching ratios from each of them; the branching ratios shown in table 1 for m/z 27 ions are the combined values for C_2H_3^+ and BCH_4^+ . Similarly, the reactant ions at m/z 26 are a mixture of isobaric ions C_2H_2^+ and $^{10}\text{BCH}_4^+$, and thus the branching ratios presented are also combined values from the two isobaric ions. Due to the high pressures used in experiments to study ion molecule reactions, the mass resolution of spectra is only high enough to distinguish certain isobaric ions of low masses, such as those mentioned above, but not high enough to distinguish the possible isobaric ions of high masses, such as the association products (ions containing two boron atoms) listed in table 1; please note that in FTMS the resolving power (ΔM) is dependent of M^2 (M is the mass of the peak). The formulae of the product ions shown in table 1 are proposed based on our reasonable guess, which are not all confirmed by the exact mass measurement; other possible isobaric ions for the same mass-to-charge ratio as the formulae shown in table 1 have not been excluded.

One can see from Table 1 that all reactant ions from TEB have slower reaction rates with neutral TEB than Ar^+ , and there is a trend of faster reaction rates for lighter reactant ions.

The reaction of Ar^+ with TEB produces $\text{BC}_4\text{H}_{10}^+$ and BC_2H_6^+ . It is expected that a dissociative charge transfer between Ar^+ and TEB produces $\text{BC}_4\text{H}_{10}^+$ and C_2H_5 , and the former in turn undergoes further dissociation forming BC_2H_6^+ by loss of C_2H_4 :

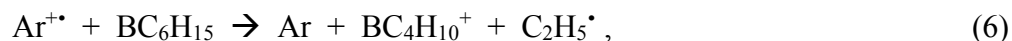


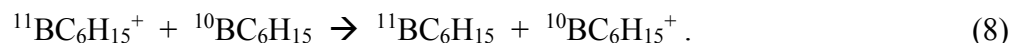
Table 1: Gas-phase Ion-molecule Reactions of TEB with Selected Ions from Electron Ionization of TEB

(Listed in the order of the increasing masses of reactant ions. Also included is the Ar⁺ reaction with TEB. Reaction rates relative to the Ar⁺ reaction, product ions and their branching ratios (in parentheses) are shown.)

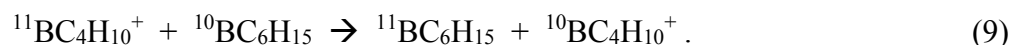
Reactant ion	Relative rate	Product ion
m/z 40 Ar ⁺	1.00	m/z 69 BC ₄ H ₁₀ ⁺ (61%) m/z 41 BC ₂ H ₆ ⁺ (39%)
m/z 26 C ₂ H ₂ ⁺	0.84	m/z 69 BC ₄ H ₁₀ ⁺ (85%) ^a m/z 41 BC ₂ H ₆ ⁺ (11%) ^a m/z 98 BC ₆ H ₁₅ ⁺ (4%) ^a
C ₂ H ₃ ⁺	0.76	m/z 69 BC ₄ H ₁₀ ⁺ (82%)
m/z 27 BCH ₄ ⁺	0.69	m/z 55 BC ₃ H ₈ ⁺ (8%) m/z 41 BC ₂ H ₆ ⁺ (7%) m/z 29 C ₂ H ₅ ⁺ (3%) m/z 69 BC ₄ H ₁₀ ⁺ (71%)
m/z 28 C ₂ H ₄ ⁺	0.54	m/z 41 BC ₂ H ₆ ⁺ (17%) m/z 98 BC ₆ H ₁₅ ⁺ (12%)
m/z 29 C ₂ H ₅ ⁺	0.61	m/z 69 BC ₄ H ₁₀ ⁺ (81%) m/z 55 BC ₃ H ₈ ⁺ (19%)
m/z 37 BC ₂ H ₂ ⁺	0.63	m/z 69 BC ₄ H ₁₀ ⁺ (84%) m/z 41 BC ₂ H ₆ ⁺ (19%) m/z 39 BC ₂ H ₄ ⁺ (3%)
m/z 39 BC ₂ H ₄ ⁺	0.62	m/z 69 BC ₄ H ₁₀ ⁺ (86%) m/z 41 BC ₂ H ₆ ⁺ (9%) m/z 108 B ₂ C ₆ H ₁₄ ⁺ (5%)
m/z 41 BC ₂ H ₆ ⁺	0.35	m/z 69 BC ₄ H ₁₀ ⁺ (100%)
m/z 53 BC ₃ H ₆ ⁺	0.32	m/z 69 BC ₄ H ₁₀ ⁺ (52%) m/z 109 B ₂ C ₆ H ₁₅ ⁺ (48%)
m/z 69 BC ₄ H ₁₀ ⁺	0.023	m/z 155 B ₂ C ₁₀ H ₁₃ ⁺ (~100%)
m/z 98 BC ₆ H ₁₅ ⁺	0.067	m/z 155 B ₂ C ₁₀ H ₁₃ ⁺ (~100%)

As seen in Table 1, $\text{BC}_4\text{H}_{10}^+$ and BC_2H_6^+ are the common and major products in many reactions: all ions smaller than $\text{BC}_4\text{H}_{10}^+$ reacting with TEB to form $\text{BC}_4\text{H}_{10}^+$, and all ions (except C_2H_5^+) smaller than BC_2H_6^+ also reacting with TEB to form BC_2H_6^+ . The mechanisms that produce these two major product ions will be discussed later. For the two hydrocarbon reactant ions, C_2H_2^+ and C_2H_4^+ , which have ionization potentials (IPs) of 11.4 and 10.507 eV, [49] respectively, which are higher than TEB (IP=9.6 eV) [49], there is a charge transfer product, $\text{BC}_6\text{H}_{15}^+$. The charge transfer product is absent in the reactions of C_2H_3^+ and C_2H_5^+ , which have IPs of 8.9 and 8.13 eV[49], respectively. For reactant ions larger than BC_2H_2^+ , there are formed the association product ions containing two boron atoms. Certain secondary product ions (not shown in table 1) due to further reactions of the primary product ions with TEB, are observed, such as m/z 87 ion (formula not identified) for the reactions of C_2H_5^+ or smaller ions. Certain minor products not listed in table 1 include ions at m/z 125 and 127 from the reaction of $\text{BC}_4\text{H}_{10}^+$ and the reaction of $\text{BC}_6\text{H}_{15}^+$ with TEB.

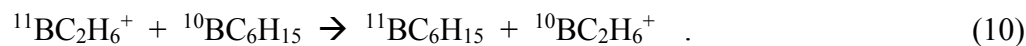
It is noteworthy to point out that when $^{11}\text{BC}_6\text{H}_{15}^+$ is isolated and reacted with a mixture of $^{11}\text{BC}_6\text{H}_{15}/^{10}\text{BC}_6\text{H}_{15}$, $^{10}\text{BC}_6\text{H}_{15}^+$ (m/z 97) was produced among other products, indicating a symmetric charge transfer reaction between $\text{BC}_6\text{H}_{15}^+$ and BC_6H_{15} :



Here a symmetric reaction means a reaction in which the products are chemically the same as the reactants and thus the enthalpy of reaction is zero if there is no isotope effect. Similarly there is a symmetric reaction of $^{11}\text{BC}_4\text{H}_{10}^+$ with $^{10}\text{BC}_6\text{H}_{15}$ producing $^{10}\text{BC}_4\text{H}_{10}^+$ (m/z 68), which cannot be explained by a dissociative charge transfer reaction because it would be endothermic. This reaction is therefore expected to proceed via a symmetric ethide (C_2H_5^-) transfer mechanism:



The ethide transfer reaction is likewise observed when $^{10}\text{BC}_4\text{H}_{10}^+$ is isolated; it reacts with $^{11}\text{BC}_6\text{H}_{15}$ forming $^{11}\text{BC}_4\text{H}_{10}^+$. It is also noteworthy to note that no other symmetric reactions are observed from other reactant ions. For example, the following symmetric reaction was not observed on BC_2H_6^+ :



The above hypothetical symmetric reaction is a C_4H_9^- transfer, and its absence appears to indicate that it is not a prospective reaction mechanism in reactions of TEB, probably due to the fact that C_4H_9^- transfer requires two boron-ligand bonds to be cleaved. As a comparison, C_2H_5^- transfer only requires one boron-ligand bond cleavage. Similar analysis of reactions of other reactant ions enables us to conclude that other alkyl transfers, except ethide transfer, also are not prospective channels in reactions of TEB.

Based on the above discussion, we propose the mechanism of forming the common product ion $\text{BC}_4\text{H}_{10}^+$ in table 1 as an ethide transfer, as shown in the following equation for the reaction of BCH_4^+ as an example:



The neutral product in **6** is expected to have a valence structure of (CH₃)-BH-(C₂H₅). One may explain the formation of BC₄H₁₀⁺ by a dissociative charge transfer, but it is not likely based on the thermochemical consideration; the reaction is endothermic, at least for certain reactant ions that have ionization potentials available in literature for enthalpy calculations. For example, for the following dissociative charge transfer:



the enthalpy of reaction $\Delta H = \text{AP}(\text{BC}_4\text{H}_{10}^+) - \text{IP}(\text{C}_2\text{H}_5) = 1.7 \text{ eV}$, where the IP value (8.13 eV) is taken from reference [49] and the AP value (9.8±0.6 eV) is taken from the threshold of BC₄H₁₀⁺ in our ionization cross section measurement data. The kinetic shift should be insignificant for BC₄H₁₀⁺ as it is one of the most abundant and most readily formed ion from electron ionization, and therefore its threshold energy is expected to be close to its AP value. A similar discussion also applies to the threshold energy of BC₂H₆⁺ which is cited below. On the other hand, if the reaction proceeds via the ethide transfer mechanism, shown in the following equation,



the enthalpy of reaction will be -2.0 eV, calculated using additional thermochemical data from reference [49].

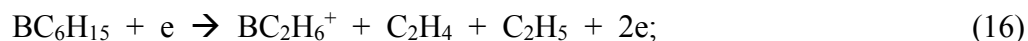
We further propose that another common product ion in table1, BC₂H₆⁺, is formed by dissociation of BC₄H₁₀⁺ (by loss of C₂H₄) after its formation from the ethide transfer. For example, the reaction of C₂H₄⁺ produces BC₂H₆⁺ via the following equation:



The above proposal is based on the following thermochemical consideration. The enthalpy of reaction (ΔH) for the equation **2** can be expressed in terms of the heat of formation ($\Delta_f H$):

$$\Delta H = \Delta_f H(\text{n-C}_4\text{H}_9) + \Delta_f H(\text{C}_2\text{H}_4) + \Delta_f H(\text{BC}_2\text{H}_6^+) - \Delta_f H(\text{C}_2\text{H}_4^+) - \Delta_f H(\text{BC}_6\text{H}_{15}). \quad (15)$$

Because the value of $\Delta_f H(\text{BC}_2\text{H}_6^+)$ is not available from the literature, we choose to use the relevant data item, the appearance energy of BC₂H₆⁺ or AP(BC₂H₆⁺), and relate it to our threshold measurement for BC₂H₆⁺, which is assumed to be formed by the following dissociative electron ionization (see the second last paragraph of section **3.1**):



$$\text{AP}(\text{BC}_2\text{H}_6^+) = \Delta_f H(\text{BC}_2\text{H}_6^+) + \Delta_f H(\text{C}_2\text{H}_4) + \Delta_f H(\text{C}_2\text{H}_5) + \Delta_f H(e) - \Delta_f H(\text{BC}_6\text{H}_{15}). \quad (17)$$

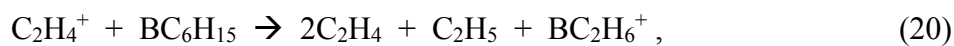
Another relevant data item, the ionization energy of C₂H₄, or IP(C₂H₄), is also used:

$$\text{IP}(\text{C}_2\text{H}_4) = \Delta_f H(\text{C}_2\text{H}_4^+) + \Delta_f H(e) - \Delta_f H(\text{C}_2\text{H}_4) \quad (18)$$

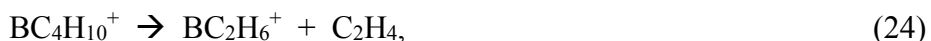
Combined with **12** and **13**, equation **10** becomes:

$$\Delta H = AP(BC_2H_6^+) - IP(C_2H_4) + \Delta_f H(n-C_4H_9) - \Delta_f H(C_2H_4) - \Delta_f H(C_2H_5) \quad (19)$$

which is calculated to be -0.1 eV, by using thermochemical data of IP and $\Delta_f H$ from reference [22] and $AP = 11.4 \pm 0.6$ eV from the threshold of $BC_2H_6^+$ in our ionization cross section measurement data. On the other hand, other reaction mechanisms to form $BC_2H_6^+$, including dissociative charge transfer and $C_4H_9^-$ transfer as shown by the following two equations, respectively, are not considered to be probable as argued later:



The neutral products in Equation 15 reflect the consecutive dissociation processes following the charge transfer, as shown by Equations 17 through 19:



in a similar manner as the dissociative electron ionization discussed in Section 3.1. While the $C_4H_9^-$ transfer process (16) is not likely as we discussed earlier (it requires two boron-ligand bonds to be cleaved), the dissociative charge transfer (15) is endothermic and therefore also unlikely. The enthalpy of reaction for Equation 15 is calculated to be: $\Delta H = AP(BC_2H_6^+) - IP(C_2H_4) = 0.9$ eV, using the IP value (10.507 ± 0.004 eV) from reference [49].

5 CONCLUSIONS

Under this three year in-house research task sponsored by the Air Force Scientific Office of Research, AFRL/RQQE researchers have successfully applied novel experimental techniques in ultraviolet laser scattering using subtractive triple-grating spectroscopy, laser diagnostics and pre-ionization using resonant multi-photon absorption and ionization, and an analysis of fuel ion chemistry using a modified Fourier transform mass spectrometer. The breadth of experimental results generated has been valuable to the assessment and development of future technological advancements for the Air Force in areas, including plasma surface treatments, laser-induced breakdown of air, and ignition enhancement.

5.1 Laser Scatter in Microplasma Conclusions

An ultraviolet laser scattering system utilizing a triple grating spectrometer has been assembled at AFRL to investigate Rayleigh, Raman, and Thomson scattering interactions in microplasma sources. This system was calibrated to obtain absolute, spatially resolved measurements of both T_g and T_r within the plasma at temperatures up to 2000 K. These measurements were obtained with spatial resolution of 150 μm and 50 μm respectively. Gas temperature measurements taken in the plasma jet indicated that the temperature is reduced to ambient over the distance of 1 cm, consistent with temperature measurements made in laminar flow. Measurements in the d.c. glow were consistent with previous temperature measurements made in d.c. glow discharges. Overall, it was observed that T_r and T_g were in agreement over the full range of the plasma. Minor discrepancies between T_g and T_r measurements in the peak temperature zones within the highest current glow discharges were most likely the result of either the increasing uncertainty of the Rayleigh technique near 2000 K or a difference in spatial resolution of the Rayleigh and Raman techniques over the narrow temperature peak. It was not ruled out, though, that T_g and T_r may actually deviate somewhat in the hottest discharge regions. Such high temperatures, however, represent the upper limit of low temperature plasma operation and are not likely to limit the application of the diagnostic to typical atmospheric plasma sources.

The Rayleigh scattering diagnostic presented here can be applied to plasma sources operating on a variety of gas species. This is aided by the fact that Rayleigh scattering cross sections for many common applications, combustion and materials processing for example, are on the same order of magnitude [6]. Raman scattering, in comparison, must be restricted to molecular gases, such as N_2 and O_2 . As discussed in section 4.1, the largest measurable temperature in this system is determined by the signal to noise ratio of the scatter intensity. Examining the expression for scatter intensity given by eq. 3, it is clear that the signal to noise ratio also determines the lower limit of gas density. For the present operating conditions, this corresponds to a minimum pressure of 0.15 atm. In the future, these limits can be improved by increasing the laser power and improving the optical transmission of the imaging system.

5.2 Laser Ignition Conclusions

Resonant laser induced breakdown of an ignition gap utilizing REMPI processes was studied for its potential to improve the spatial and temporal precision of arc ignition in aircraft combustion. Two parallel electrodes were configured as an air or air-propane flow gap and were connected in series with a capacitor charged to several tens of thousands of volts. A pulsed ultraviolet laser, at a wavelength of 287.5 nm, was propagated co-axially through a small aperture in the anode. The ionization caused by the laser produced a channel of free charge

between the electrodes, inducing electron avalanche and igniting the arc. Laser-induced breakdown and ignition by this method was accomplished with an applied voltage as low as 33% of the voltage required for self-breakdown. The evolution of the breakdown process between the laser pulse and the arc formation was studied by high speed imaging and spectroscopy. Findings include that the initial ionization is centered at the laser focus, but space charge effects and field enhancements are dynamic throughout the arc delay period, leading to a high temperature arc event along the initial laser path. The development of this novel scheme could result in a compact, low-power laser ignition system with a lower voltage ignition source.

5.3 Ion Chemistry of Fuels Conclusions

With exact mass measurements using FTMS, the product ions from electron ionization of TEB in the energy range of from 6.6 to 200 eV have been identified as $C_2H_{2-5}^+$, BCH_4^+ , $BC_2H_{2,4,6}^+$, $BC_3H_{4,6}^+$, $BC_4H_{8,10}^+$ and $BC_6H_{15}^+$. The heavy product ions (m/z 37 or heavier) are exclusively boron-carbon species, while the light ions are all non-boron-containing species except a boron-containing isobaric ion at m/z 27. The major product ions in the energy range studied are the parent ion $BC_6H_{15}^+$ and fragment ions $BC_4H_{10}^+$ and $BC_2H_6^+$. The absolute total and partial ionization cross sections are measured. The total cross section is found to peak at a value of $2.2 \times 10^{-15} \text{ cm}^2$ in the electron energy region of 65-85 eV.

Gas-phase reactions between TEB and certain major ions from the electron ionization of TEB are studied. A trend is observed that faster reaction rates result from lighter reactant ions. Product ions $BC_4H_{10}^+$ and $BC_2H_6^+$ are found to be common among reactions of small reactant ions (smaller than $BC_3H_6^+$), while association product ions are significant for the large reactant ions. Symmetric reactions are observed for reactant ions $BC_6H_{15}^+$ and $BC_4H_{10}^+$. Based on this observation and on the thermochemical consideration, the reaction mechanisms forming the two common product ions, $BC_4H_{10}^+$ and $BC_2H_6^+$, are proposed to be simple ethide transfer and ethide transfer followed by dissociation (loss of C_2H_4), respectively.

6 REFERENCES

- [1] K. Becker, K. Schoenbach and J. Eden, "Microplasmas and applications," *J. Phys. D: Appl. Phys.*, Vol. 39 (2006) R55-R70.
- [2] K. Becker, A. Koutsospyros, S. M. Yin, C. Christodoulatos, N. Abramzon, J. C. Joaquin and G. Brelles-Marino, "Environmental and biological applications of microplasmas," *Plasma Phys. Control. Fusion*, Vol. 47 (2005) B513-B523.
- [3] E. Carbone and S. Nijdam, "Thomson scattering on non-equilibrium low density plasmas: principles, practice and challenges," *Plasma Phys. Control. Fusion*, Vol. 57, No. 1 (2015) 014026.
- [4] B. Van Gessel, R. Brandenburg and P. Bruggeman, "Electron properties and air mixing in radio frequency driven argon plasma jets at atmospheric pressure," *Appl. Phys. Lett.*, Vol. 103, No. 6 (2013) 064103.
- [5] V. Donnelly, S. Belostotskiy, D. Economou and N. Sadeghi, "Laser thomson scattering, Raman scattering, laser-absorption diagnostics of high pressure microdischarges," *Journal of Physics: Conference Series*, Vol. 227, No. 14th International Symposium on Laser-Aided Plasma Diagnostics (2010) 012011.
- [6] D. Long, Raman Spectroscopy, New York: McGraw-Hill, 1977.
- [7] X. Deng, A. Nikiforov, P. Vanraes and C. Leys, "Direct current plasma jet at atmospheric pressure operating in nitrogen and air," *Journal of Appl. Phys.*, Vol. 113, No. 2 (2013) 023305.
- [8] J.D. Few and J.W.L. Lewis, "Laser initiated non-linear fuel droplet ignition," University of Tennessee Research Corporation: USA, 1997.
- [9] B. Chehroudi, "Laser Ignition for Combustion Engines," *Proceedings of the Advanced Laser Applications Conference and Exposition*, Ann Arbor, MI, 2004.
- [10] S.F. Adams, J.A. Miles, and A.C. Laber. "Resonant Laser-Induced Breakdown for Fuel Air Ignition," *Proceedings of the 48th AIAA Aerospace Sciences Meeting*, Orlando, FL, 2010.
- [11] S.F. Adams, "Low Energy Laser-Induced Ignition of Air-Fuel Mixture", US Air Force: Patent: USA, 2010.
- [12] J. Mayes and W. Carey. "Compact Pulsed Power Sources," *SAE Power Systems Conference*, Coral Springs FL, 02PSC-25, October 2002.
- [13] O. Frolov et al., "Gas-Filled Laser-Triggered Spark Gap." *Czechoslovak J. of Phys.*, Vol. 54, Supplement C (2004) C309-C313.
- [14] Y. Wu, Z. Zhang, and S.F. Adams "O₂ Rotational Temperature Measurements by Coherent Microwave Scattering from REMPI" *Chem Phys. Lett.*, Vol. 513 (2011) 191-194.
- [15] R.E. Williams, "The polyborane, carborane, carbocation continuum: architectural patterns", *Chem. Rev.*, Vol. 92 (1992) 177.

- [16] J. Plešek, "Potential applications of the boron cluster compounds", *Chem. Rev.*, Vol. 92 (1992) 269.
- [17] S. Hermanek, "Boron Chemistry: Introduction", *Chem. Rev.*, Vol. 92 (1992) 175.
- [18] B. Gruner, B. Stibr, "15th International Conference on Boron Chemistry", *Pure Appl. Chem.*, Vol. 87 (2015) 121.
- [19] Y. Li, J. Liu, L. Zhang, L. Zhu, J. Hu, "Radical (Phenylsulfonyl)difluoromethylation with Iododifluoromethyl Phenyl Sulfone", *J. Org. Chem.*, Vol. 72 (2007) 5824.
- [20] J. Boivin, V.T. Nguyen, "Triethylborane-air: a suitable initiator for intermolecular radical additions of S-2-oxoalkyl-thionocarbonates (S-xanthates) to olefins", *Beilstein J. Org. Chem.*, Vol. 3 (2007) No. 47.
- [21] P. Panchaud, P. Renaud, "Tin-free radical carboazidation", *Chimia*, Vol. 58 (2004) 232.
- [22] L. Liu, X. Wang, C. Li, "Deoligomerization: A new route to lactams from unsaturated amides via radical oligomerization", *Org. Lett.*, Vol. 5 (2003) 361.
- [23] C. Ollivier, P. Renaud, "Organoboranes as a Source of Radicals", *Chem. Rev.*, Vol. 101 (2001) 3415.
- [24] S.A. Whimore, D.P. Merkley, S.D. Eilers, M.I. Judson, "Development and Testing of a Green Monopropellant Ignition System", 49th AIAA/ASME/SAE/ASEE Joint Propulsion Conference and Exhibit, San Jose, CA, 15-17 July 2013.
<http://ntrs.nasa.gov/archive/nasa/casi.ntrs.nasa.gov/20140002595.pdf>
- [25] C.S. Tsai, D.P. Yen, J.J. Chiou, *Huoyao Jishu*, Vol. 7 (1991) 1.
- [26] K.R. Kline, K.W. Smith, "Hybrid Rocket Motor having a Precombustion Chamber", Patent Application Publication, US 2003/0136107 A1, Jul. 24, 2003.
- [27] N.V. Sutton, H. Schneider, "Analysis of hypergolic igniters", *Microchem. J.*, Vol. 9 (1965) 209.
- [28] N. Bibinov, D. Dudek, P. Awakowicz and J. Engemann, "Characterization of an atmospheric pressure dc plasma jet," *J. Phys. D: Appl. Phys.*, Vol. 40, No. 23 (2007) 7372-8.
- [29] D. Dudek, N. Bibinov, J. Engemann and P. Awakowicz, "Direct current plasma jet needle source," *J. Phys. D: Appl. Phys.*, Vol. 40, No. 23 (2007) 7367-71.
- [30] A. Mohamed, J. Kolb and K. Schoenbach, "Low temperature, atmospheric pressure, direct current microplasma jet operated in air, nitrogen, and oxygen," *Eur. Phys. J. D*, Vol. 60, No. 3 (2010) 517-522.
- [31] S. Adams, J. Caplinger and B. Sommers, "Spatial temperature mapping of an atmospheric plasma using ultraviolet Rayleigh scatter imaging," *Plas. Sources Sci. Technol.*, Vol. 24, No. 2 (2015) 025031.
- [32] M. Van de Sande, *Laser Scattering on Low Temperature Plasmas*, Netherlands: Eindhoven, University of Technology, 2002.

- [33] S. Belostotskiy, Q. Wang, V. Donnelly and D. Economou, "Three-dimensional gas temperature measurements in atmospheric pressure microdischarges using Raman scattering," *Appl. Phys. Lett.*, Vol. 89 (2006) 251503.
- [34] S. Zhang, W. Van Gaens, B. Van Gessel, S. Hofmann, E. Van Veldhuizen, A. Bogaerts and P. Bruggeman, "Spatially resolved ozone densities and gas temperatures in a time modulated RF driven atmospheric pressure plasma jet," *J. Phys. D: Appl. Phys.*, Vol. 46 (2013) 205202.
- [35] Van Gessel, E. Carbone, P. Bruggeman and J. Van der Mullen, "Laser scattering on an atmospheric pressure plasma jet: disentangling Rayleigh, Raman, and Thomson scattering," *Plasma Sources Sci. Technol.*, Vol. 21 (2012) 015003.
- [36] S. Hassaballa, M. Yakushiji, Y. Kim, K. Tomita, K. Uchino and K. Muraoka, "Two-dimensional structure of PDP micro-discharge plasmas obtained using Laser Thomson Scattering," *IEEE Trans. on Plas. Sci.*, Vol. 32, No. 1 (2004) 127-34.
- [37] B. Saleh and M. Teich, Fundamentals of Photonics, 2nd Edition, New York: Wiley, 2007, p. Chapter 3.
- [38] C. Palmer, Diffraction Grating Handbook, 5th Edition, Rochester, New York: Richardson Grating Laborator, 2002.
- [39] C.Q. Jiao, C.A. DeJoseph, Jr., A. Garscadden, "Ion chemistries in hexamethyldisiloxane", *J. Vac. Sci. Technol. A* Vol. 23 (2005) 1295.
- [40] S. Guan, "General phase modulation method for stored waveform inverse Fourier transform excitation for Fourier transform ion cyclotron resonance mass spectrometry", *Chem. Phys.* Vol. 91 (1989) 775.
- [41] H.C. Straub, P. Renault, B.G. Lindsay, K.A. Smith, R.F. Stebbings, "Absolute partial and total cross sections for electron-impact ionization of argon from threshold to 1000 eV" *Phys. Rev. A*, Vol. 52 (1995) 1115.
- [42] R.C. Wetzel, F.A. Baiocchi, T.R. Hayes, R.S. Freund, "Absolute cross sections for electron-impact ionization of the rare-gas atoms by the fast-neutral-beam-method" *Phys. Rev. A* Vol. 35 (1987) 559.
- [43] NIST Mass Spec Data Center, S.E. Stein, director, "Mass Spectra" in *NIST Chemistry WebBook, NIST Standard Reference Database Number 69*, Eds. P.J. Linstrom and W.G. Mallard, National Institute of Standards and Technology, Gaithersburg MD, 20899, <http://webbook.nist.gov>, (retrieved September 2, 2014).
- [44] G. Herzberg, Molecular Spectra and Molecular Structure I. Spectra of Diatomic Molecules, Malabar, FL: Krieger, 1989.
- [45] D. Staack, B. Farouk, A. Gutsol and A. Fridman, "DC normal glow discharges in atmospheric pressure atomic and molecular gases," *Plasma Sources Sci. Technol.*, Vol. 17 (2008) 025013.
- [46] Shapiro, C.O. Wilson, J.F. Ditter, W.J. Lehmann, "Mass Spectrometry in Boron Chemistry", *Adv. Chem. Ser.*, Vol. 32 (1961) 127-138.

- [47] C.Q. Jiao, S.F. Adams, "Electron Ionization of Selected Cyclohexanes", *J. Phys. B: At. Mol. Opt. Phys.*, Vol. 44 (2011) 175209.
- [48] C.Q. Jiao, C.A. DeJoseph Jr., A. Garscadden, S.F. Adams, "Gas-Phase Ion Chemistries in Perfluoromethylcyclohexane", *Plasma Sources Sci. Technol.* Vol. 18 (2009) 025007.
- [49] S.G. Lias, J.E. Bartmess, J.F. Liebman, J.L. Holmes, R.D. Levin, W.G. Mallard, "Gas-Phase Ion and Neutral Thermochemistry", *Journal of Physical and Chemical Reference Data*, Vol. 17, (1988).